

Soot Particle Size Distribution of a Microflow Tube Reactor : Experimental and Sectional Modeling Investigations

A Thesis

Presented to

the faculty of the School of Engineering and Applied Science

University of Virginia

in partial fulfillment

of the requirements for the degree

Master of Science in Mechanical and Aerospace Engineering

by

Rohit Singhal

August

2015

APPROVAL SHEET

The thesis
is submitted in partial fulfillment of the requirements
for the degree of
Master of Science in Mechanical and Aerospace Engineering

Rohit Singhal

Author

The thesis has been read and approved by the examining committee:

Prof. Christopher Goyne

Committee Chairman

Prof. Harsha Chelliah

Advisor

Prof. Haibo Dong

Accepted for the School of Engineering and Applied Science:

Dean, School of Engineering and Applied Science

August
2015

Abstract

The adverse health, environmental, and climatic effects of soot particulate emissions are well known. Extensive research has been conducted to understand the fundamental mechanisms of soot particle formation, namely nucleation, growth, and oxidation, but these processes under realistic conditions are still not completely understood due to insufficient experimental data. In this work, a Scanning Mobility Particle Sizer (SMPS) with a nano-differential mobility analyzer (n-DMA) is utilized for real time sampling and measurement of nascent soot particles in the size range of 3-100 nm over a range of temperatures and residence times.

The flow reactor employed consists of a novel micro-flow tube reactor (MFTR) developed at UVa with provision for feeding any fuel mixed with a carrier inert gas, typically nitrogen heated to a target temperature (<1200 K). For soot oxidation investigations, the fuel stream can be mixed with oxygen. In the present initial investigation, the fuel considered was ethylene as it is the primary product of fast thermal pyrolysis of large hydrocarbon molecules used in propulsion systems. With the SMPS system and the probing approach developed, soot particle size distributions (PSDs) were obtained for a range of temperatures and residence times during pyrolysis and oxidation of ethylene in MFTR. Unlike other laboratory flames investigated with the SMPS showing bimodal distributions of nascent soot, the present PSDs for ethylene pyrolysis and oxidation shows a normal distribution with a single mode. As expected, the soot particles mass and number density is shown to increase with increase in flow residence time at a constant temperature. The residence times were varied from 150 to 600 ms over a range of temperature from 1100 to 1200 K to define the temperature and residence time limits that lead to onset of soot formation under ethylene pyrolysis conditions. Ethylene oxidation was also studied for two equivalence ratios and it was found that the particles were concentrated towards smaller sizes indicating substantial decrease in soot growth rates.

The experiment results were also compared to the results obtained from a zero dimensional numerical model with soot particle nucleation, growth, and oxidation described by discrete sectional approach, for both oxidation and pyrolysis cases. For soot nucleation, pyrene was treated as the monomer that leads to formation of soot nuclei. There

was a general agreement between the experiment and the model results with respect to trends in total soot particle mass and number concentrations over the range of residence times in the case of pyrolysis of ethylene. In the oxidation case, the mode and the mean diameter of the size distribution agreed well in experimental and model results.

Acknowledgements

My sincerest gratitude to my advisor, Dr. Harsha Chelliah, for entrusting me with this opportunity and for his insights and guidance in the course of this research.

I am also grateful to Dr. Gaetano Esposito and Dr. Chowdhury Moniruzzaman for their help in the model development work. I also want to thank all my colleagues in the lab, especially Ujuma Shrestha for getting me started with the SMPS machine.

This work was supported by Rolls Royce and the Commonwealth Center for Aerospace Propulsion Systems, with Dr. MS Anand at Rolls Royce as the technical monitor.

Lastly, I would like to thank my family and friends for their invaluable support.

Contents

Abstract	i
Acknowledgements	iii
Contents	iv
List of Figures	vi
List of Tables	viii
Abbreviations	ix
Symbols	x
1 Introduction	1
1.1 Literature Review	2
1.2 Study of Soot Formation and Growth	4
1.2.1 Surface Growth	4
1.2.2 Oxidation of Aromatics and Soot Particles	5
1.2.3 Soot Growth through Coagulation	5
1.3 Motivation	6
1.4 Outline of Thesis	8
2 Laboratory Experimental Set-Up	9
2.1 Laboratory Set-UP of Reactors	9
2.1.1 Set-Up for Burner Stabilized Flat Flame	9
2.1.2 Set-up for Micro-flow Tube Reactor (MFTR)	11
2.2 Scanning Mobility Particle Sizer	13
2.2.1 Mobility Diameter	17
2.3 Calibration of Orifice Flow Rate	17
2.4 Summary	20
3 Mathematical Model of PSDF	22
3.1 Gas Phase Reaction Model	23
3.2 Particle Nucleation and Growth Model	24
3.2.1 Collision Frequency Coefficient	25
3.2.2 Nucleation	26

3.2.3	Coagulation	27
3.2.4	Surface Growth	28
3.2.4.1	HACA Mechanism and Oxidation	28
3.2.4.2	PAH Condensation	30
3.2.4.3	Implementation of Surface Growth	31
3.3	Implementation	32
3.4	Summary	33
4	Results	34
4.1	PSDF from a flat flame burner	35
4.1.1	Dilution ratio and its effect on measured PSDF	35
4.1.2	Absolute PSDF	36
4.2	PSDF from Fuel Pyrolysis in Atmospheric MFTR	39
4.2.1	Dilution ratio	39
4.2.2	Absolute PSDFs	42
4.3	PSDF from Ethylene Oxidation in MFTR	45
4.4	Uncertainties in the experiment	46
4.5	Results from the Particle Nucleation and Growth Model	48
4.5.1	Case1: Pyrolysis	49
4.5.2	Case2: Oxidation	50
4.6	Summary	52
5	Conclusions	54
5.1	Future Work	55
	References	56

List of Figures

1.1	Schematic of soot formation process [1]	3
2.1	Schematic of experiment set-up for burner stabilized flat-flame	10
2.2	Schematic of experiment set-up for micro-flow atmospheric tube reactor (MFTR)	12
2.3	Cross-Sectional view of Inertial Impactor [2]	14
2.4	Flow schematic for the Electrostatic Classifier with nano-DMA in dual-blower mode [3]	15
2.5	Flow schematic for the nano-CPC [4]	16
2.6	Relation between particle diameter and the mobility diameter	18
2.7	Experimental Flow rate through orifice versus differential pressure across orifice for 250 μ m orifice	18
2.8	Variation of entrance length of flow through 250 μ m orifice with variation in pressure across orifice	19
2.9	Comparison of experimental flow rate and calculated flow rate through orifice as a function of differential pressure across orifice for 250 μ m diameter for different temperatures	20
2.10	Comparison of experimental flow rate and calculated flow rate through orifice as a function of differential pressure across orifice for 130 μ m diameter at 298 K	21
4.1	Variation of dilution ratio (f_D) with the variation in differential pressure across 130 μ m orifice for a carrier gas N_2 flow rate of 42 lpm	35
4.2	Absolute PSDF at HAB = 0.81cm for three dilution ratios at a fixed equivalence ratio, $\phi = 2.1$	36
4.3	Absolute PSDF at HAB = 0.76 cm at a fixed $\phi = 2.1$	37
4.4	Absolute PSDF at increasing heights above the burner surface at a fixed $\phi = 2.1$	38
4.5	Absolute PSDF at HAB = 0.91cm at a fixed $\phi = 2.1$	39
4.6	Mean diameter of soot particles as a function of HAB at a fixed $\phi = 2.1$	40
4.7	Variation of dilution ratio with the variation in differential pressure through 250 μ m orifice for a carrier gas N_2 flow rate of 20 lpm and 40 lpm	41
4.8	Soot PSDF obtained from 2% ethylene pyrolysis at 1200 K with residence time of 600 ms inside the MFTR	41
4.9	Soot PSDF for ethylene pyrolysis at 1200 K for a range of residence time	42
4.10	Soot PSDF obtained at temperatures ranging from 1150 to 1200 K. The residence time is the earliest residence time at which soot PSDF are obtained in SMPS	43

4.11	The earliest residence times at which soot PSDF are obtained in SMPS are plotted as the function of corresponding temperature	44
4.12	Soot PSDF obtained from 2% ethylene pyrolysis at 600ms residence time for 1200K and 1150K	44
4.13	Soot PSDF obtained for the case of ethylene oxidation at 1200K and 500ms residence time	45
4.14	Comparison of soot PSDF for the cases of ethylene oxidation and pyrolysis	45
4.15	Counting efficiency curve of CPC [5]	47
4.16	Soot PSDF and the uncertainty bar at each particle size, obtained from pyrolysis of ethylene at 1200 K and 600 ms residence time	48
4.17	Soot PSDF and the uncertainty bar at each particle size, obtained from oxidation of ethylene at 1200 K and 500 ms residence time with $\phi = 5.0$.	48
4.18	Total number concentration as a function of residence time for the case of ethylene pyrolysis at 1200K from model simulations and experimental measurements	49
4.19	Total mass concentration as a function of residence time for the case of ethylene pyrolysis at 1200K from model simulations and experimental measurements	50
4.20	Soot PSDF obtained for the case of ethylene pyrolysis, at 1200K and 600ms residence time, from model simulations and experimental measurements	50
4.21	Normalized soot PSDF obtained for the case of ethylene pyrolysis, at 1200K and 600ms residence time, from model simulations and experimental measurements	51
4.22	Soot PSDF at equivalence ratios, 4.5 and 5.0, at 1200K and 500ms residence time, obtained from model simulation and experimental measurements	51
4.23	Normalized soot PSDF at equivalence ratios, 4.5 and 5.0, at 1200K and 500ms residence time, obtained from model simulations and experimental measurements	52

List of Tables

3.1	Soot Surface Growth Mechanism	29
3.2	Input variables of the model	32
4.1	Mean Diameter of the particles at different Residence Times	42

Abbreviations

<i>BSFF</i>	Burner Stabilized Flat Flame
<i>ER</i>	Equivalence Ratio
<i>HAB</i>	Height Above the Burner surface
<i>HACA</i>	Hydrogen Abstraction and C_2H_2 Addition
<i>ID</i>	Internal Diameter
<i>lpm</i>	Litres per Minute
<i>MFTR</i>	Micro-Flow Tube Reactor
<i>n-CPC</i>	nano-Condensation Particle Counter
<i>n-DMA</i>	nano-Differential Mobility Analyzer
<i>n-WCPC</i>	nano-Water based Condensation Particle Counter
<i>OD</i>	Outer Diameter
<i>PAHs</i>	Polyaromatic Hydrocarbons
<i>PBE</i>	Population Balance Equation
<i>PDFs</i>	Particle Distribution Functions
<i>PFR</i>	Plug Flow Reactor
<i>PSDFs</i>	Particle Size Distribution Functions
<i>PSR</i>	Perfectly Stirred Reactor
<i>SMPS</i>	Scanning Mobility Particle Sizer
<i>WSR</i>	Well Stirred Reactor

Symbols

A	Area of cross-section of probe orifice
A_k	Pre-exponential constant in the Arrhenius equation of the k_{th} reaction.
A_v	Avogadro number
c_i	Thermal velocity of particle in i_{th} bin
$coag$	Coagulation
C	Cunningham slip correction factor
$C_{c,i}$	Cunningham slip correction factor of particles in bin i
$chem$	Chemical reaction
d_i	Diameter of particle in i_{th} bin
d_{Kelvin}	Kelvin diameter
D_{50}	Cut-point diameter at which particles are separated in Impactor
D_i	Diffusion coefficient of particle in i_{th} bin
D_p	True diameter obtained from mobility diameter measured by SMPS
$D_p^{mobility}$	Mobility diameter measured by SMPS
e	Elementary charge (1.6×10^{-19} <i>Coulomb</i>)
E_k	Activation energy of the k_{th} reaction in the Arrhenius equation.
f_D	Dilution ratio
f_v	Ratio of particles sizes from two consecutive bins
f_w	Factor to account for diffusive wall losses
g_i	Characteristic length of particle in i_{th} bin
gr	Surface growth
I_i	Rate of change in particle volume in bin i due to surface growth
k	Boltzmann constant
k_f	Rate constant of a forward reaction
k_b	Rate constant of a backward reaction

Kn	Knudsen number
l_i	Mean free path of particle in i_{th} bin
m_C	the mass of one atom of carbon
m_k	Mass of the k_{th} species
m_i	Mass of a particle in i_{th} bin
m_r	Reduced mass
M_{pyrene}	Molecular mass of pyrene
$nucl$	Nucleation
n	molar concentration
N	Soot particle number density measured by SMPS
$N(v, t)$	Particle size distribution at time t
N_a	Absolute number density of particles
N_i	Number density in i_{th} bin
N_r	Total number of reactions
N_{sp}	Total number of species
N_{bins}	Total number of bins
N_k	Number density in k_{th} bin
P	Pressure
P_s	Saturation vapor pressure
Q_c	Flow rate of carrier gas N_2 through the sampling probe
Q_0	Flow rate through the orifice of the probe
R	Universal gas constant
$(SA)_i$	Surface area of particles representing bin i
Stk	Stokes number
$S(v)$	Nucleation rate of particle of volume v
t	Time
T	Temperature
T_r	Ratio of inlet gas temperature and carrier gas temperature
v_{sp}	Specific volume
v, v'	Volume of particles in a section
v_k	volume of particles representing k_{th} bin
v_0	volume of particles representing first bin
V	volume

W	Nozzle diameter of Impactor
W_k	Molecular weight of the k_{th} species
Y_k	Mass fraction of the k_{th} species
Z	Electrical mobility
α_{coag}	Collision efficiency in Coagulation
α_{cond}	Collision efficiency in Condensation
α_{nucl}	Collision efficiency in Nucleation
β	Collision frequency
β_k	Temperature exponent in the Arrhenius equation of the k_{th} reaction
$\beta(v, v')$	Collision frequency of two particle of volume v and v'
$\beta_{i,j}$	Collision frequency of particles representing bin i and bin j
$\delta_{j,k}$	Kronecker delta function
$\omega_{avg}^{(1,1)*}$	Average reduced collision integral
λ	Mean free path
ΔP	Pressure difference across the probe orifice
μ	Gas viscosity
γ	Surface tension
ρ	Density
ρ_c	Density of condensing fluid in n-CWPC
$\dot{\omega}_k$	Molar production or depletion rate of the k_{th} species
$\eta_{j,k}$	Partition coefficient to distribute new particles to neighboring bins during coagulation

Chapter 1

Introduction

Combustion plays a major role in almost all the essential human activities ranging from cooking, home heating, manufacturing, power generation, and material synthesis. Combustion of fossil fuels is by far the most predominant (more than 80%) source of energy and will likely remain significant for many years to come [6].

Soot is a particulate matter formed during combustion of fuel under conditions which allows polymerization and condensation of fuel [7]. Soot formation has been an active field of combustion research not just because it remains a challenge from a fundamental point of view, but also because combustion-generated soot particles exhibit significant health and environmental effects [8].

Release of soot into the atmosphere causes significant environmental and health hazards. Soot particles are commonly identified as carbonaceous particles that are roughly 2 nm or greater in effective diameter [9]. Because of their small sizes soot particles emitted into atmosphere and inhaled by humans can deposit on the lungs causing diseases such as asthma, bronchitis, and lung cancer. A possible explanation for these effects is the association of soot particles with the polycyclic aromatic hydrocarbons (PAH) which are carcinogenic and mutagenic and are able to deposit on soot surface and therefore travel with soot particles, causing additional damage to the respiratory system [10–12]. The amount of different PAHs associated with various sizes of soot particles have been studied to obtain a better understanding of their relation with the human exposure [13–17].

From the environmental perspective, soot emission can significantly degrade air quality such as reducing visibility. Soot emission is also closely related to global warming as soot is a strong absorber of solar energy. Newly emitted soot particles can survive in the atmosphere for several weeks before settling on the ground. These particles are often transported over long distances, mixing with other aerosols along the way. The aerosol mix can form transcontinental plumes of atmospheric brown clouds, with vertical extents of 3 to 5 *km*. Emissions of soot particles are the second strongest contribution to current global warming, after carbon dioxide emissions [18, 19].

1.1 Literature Review

Soot formation is a complex process which involves a number of chemical and physical steps. There is a general agreement among the researchers on the reaction path that leads to the formation of soot in flames. These steps include the molecular precursor formation, particle nucleation, coagulation, soot growth and condensation as shown in Fig. 1.1 [20–24]. Even though this reaction pathway has been well accepted, the formation of the first aromatic ring and particle inception is still of great interest among researchers as it involves the transition from gas-phase to solid.

Several pathways have been proposed to explain the soot particle inception which include polyacetylenes, ionic species or the polycyclic aromatic hydrocarbons (PAH) as the key gaseous precursors to soot. Homann and Wagner [25, 26] considered that polyacetylenes play a significant role during soot precursors and proposed a mechanism which explains the formation of large hydrocarbon molecules due to the reactions of large radicals with themselves and with polyacetylenes to form even larger molecules. This mechanism came under criticism by Calcote [27] who argued that reactions of neutral species are not fast enough and proposed a reaction pathway through ionic mechanism where chemi-ions are the precursors on which free radicals, polyacetylenes and PAH repeatedly add through fast ion-molecule reactions. Frenchlach et al. [23] disproved Calcote's arguments and argued that detailed kinetic simulations identified the HACA thermodynamic-kinetic coupling as a responsible factor for the growth of molecular mass on the scale seen in experiments. They also showed that the effect of thermodynamic and kinetic barriers on the growth of neutral species should apply equally to the growth of ionic species.

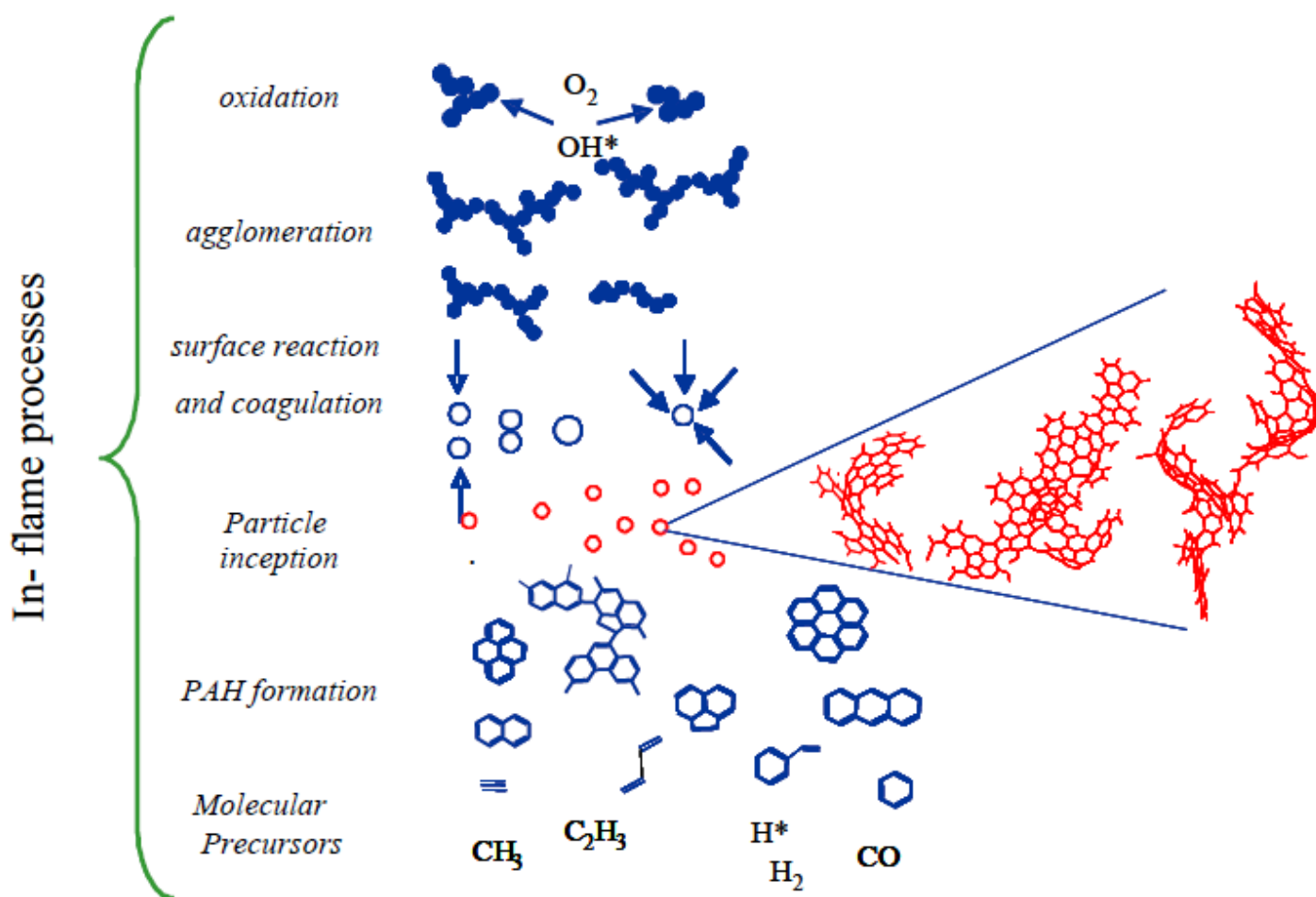


FIGURE 1.1: Schematic of soot formation process [1]

In the initial work by Frenchlach et al. [23], the transition from gaseous species to solid particles was considered purely chemical, i.e. mass accumulated on PAH species to form a large PAH was called soot. This mechanism was able to account for the amount of soot mass formed but underpredicted the particle sizes. In the follow-up work [28], they proposed the accumulation of particle mass via (1) chemical reactions with gaseous precursors and (2) simultaneous growth of particle size due to collisions among PAH molecular species. This mechanism was ruled out by Miller et al. [29] based on the dimers concentration for small soot particles in flames.

Supported by numerous experimental and modeling studies, it is widely accepted that soot particles form via PAHs through formation of aromatic aliphatic linked hydrocarbons which later graphitize [30, 31]. The formation of aromatic compounds from small aliphatic molecules is a relatively slow step but the aromatics formed can undergo rapid

polymerization to form or grow soot via hydrogen abstraction and acetylene addition (HACA). Hence, the formation of first aromatic ring from aliphatic molecules is considered as the rate limiting step [24, 28, 32–36].

Several possibilities have been proposed to explain the formation of first aromatic ring. Among these are the even-carbon atoms and the odd-carbon atoms pathway. In the even-carbon pathway, acetylene reacts with $n - C_4H_3$ or $n - C_4H_5$ to form phenyl or benzene [23, 28]. This mechanism was dismissed by Miller and Melius [35] who argued that $n - C_4$ radicals vanish quickly due to their rapid transformation to their resonantly stabilized isomers ($iso - C_4H_3$ and $iso - C_4H_5$). In the odd-carbon pathway proposed by Miller and Melius [35] and others [33, 34], the propargyl [C_3H_3] radical combines with itself and undergo cyclization steps that lead to benzene or phenyl formation. This mechanism was, however, shown to be highly dependent on fuel and flame type by McEnally et al. [37] and Sidebothan et al. [38]. A D’Anna and Violi [39, 40] proposed a combination reaction of 1-methylallenyl and propargyl with the formation of benzyl radicals and their subsequent decomposition to benzene. They suggested that $n - C_4H_3$ and $n - C_4H_5$ (part of standard reaction for benzene formation) get easily converted to the more stable isomers, and therefore their concentration is too low to account for the benzene in concentration flames. Hence, the presence of high concentration of benzene suggest a new pathway for benzene formation.

1.2 Study of Soot Formation and Growth

1.2.1 Surface Growth

As soon as the first PAH species is formed, it undergoes growth reactions leading to formation of large PAH molecules. One of the most accepted surface growth mechanism is HACA (Hydrogen-abstraction- C_2H_2 -addition) mechanism proposed by Frenchlach and Wang [20]. This is a repetitive reaction mechanism involving two principle step (*i*) abstraction of a hydrogen atom from the reacting PAH by a gaseous hydrogen atom to form a PAH radical and (*ii*) addition of gaseous acetylene to the PAH radical. In this mechanism the H abstraction by gaseous H atom is the dominating step. Recently, Parkar et al. [41] probed the phenylacetylene (C_8H_8) intermediate together with naphthalene ($C_{10}H_8$) by photo-ionization mass spectrometry during combustion conditions.

The experiments provided compelling evidence that the naphthalene along with phenylacetylene can be formed from phenyl radicals and acetylene precursors by the HACA pathway during pyrolic combustion conditions.

Several other reaction pathways and species have been proposed to propagate the growth of aromatic rings which include methyl, propargyl and cyclopentadienyl [36, 39, 40, 42, 43].

1.2.2 Oxidation of Aromatics and Soot Particles

Oxidation of PAH occur simultaneously with the growth process of aromatics. The largest effect of oxygen is understood to be at the very beginning of the aromatics growth (at the phenyl stage) as the availability of O_2 decreases in a fuel rich environment with sustained aromatics growth [44]. This was explained by Frenklach [24] in the review paper using HACA mechanism. The aromatics growth is governed by H atom production but H atoms also consume O_2 , hence as the aromatics growth progresses, the concentration of O_2 decreases indicating major impact of oxidation near beginning of aromatic growth. OH plays a minor role in the oxidation of aromatics but are considered as the primary oxidizing agents of soot particles [24, 44].

1.2.3 Soot Growth through Coagulation

As the soot particles are formed, they collide and stick with each other forming larger particles through a process called coagulation. The particles initially look spherical (explained via particle-particle coalescence) but later acquire fractal shapes (explained via agglomeration).

The coalescent growth is described by Smoluchowski coagulation equation [45] with the collision coefficients dependent on the size of the colliding particles [46, 47]. The collision coefficient are also dependent on the Knudsen number which is the ratio of the mean free path to the particle radius. The coalescence occurs primarily through free molecular regime at low pressure conditions while at high pressure continuum regime dominates [48, 49].

Particle agglomeration is the planar growth (fractal geometry) of soot particle size due to formation of chain like structures in the later stages of soot growth. The transition from spherical soot particles to fractal structures is explained through different mechanism. It is assumed by Prado et al. [50] that particles are composed of viscous matter that coalesce completely at small sizes but time is not enough for fusion at large particle sizes. Another theory proposed was that the spherical soot growth is the result of coagulation and surface growth and fractal soot structure form due to termination of surface growth [51, 52].

Soot and PAH formation are affected by several operating conditions including reaction temperature and residence time [53]. Studies [54] have shown that pyrolysis of fuel using acetylene as a direct soot precursor results in majority of PAH formation under temperature conditions from 1073 to 1223 K while majority of soot forms at higher temperatures. Experiments conducted by Sanchez et. al. [55] found correlation of temperature and residence time in the production of PAH and soot particles. Low reaction temperature showed limited influence on PAH formation irrespective of residence time while at intermediate reaction temperature, residence time showed strong effect on PAH formation. It was also found that at high reaction temperature, increase in residence time resulted in low amount of PAH due to formation of soot particles.

1.3 Motivation

To better understand the soot formation in combustion systems, a detailed measurement of soot particle size distributions is required under conditions of incipient particle formation. These measurements are required to validate the numerical models of soot formation in flames and tube reactor. In recent years several novel experimental techniques like small-angle X-ray scattering [56, 57], small-angle neutron scattering [58] and scanning mobility particle sizer (SMPS) [59–61] have been used to understand the formation of incipient soot particles and their subsequent growth.

The goal of this study was to measure the soot particle size distribution function (PSDF) in a micro-flow tube reactor (MFTR) through the online sampling procedure using the nano-Scanning Mobility Particle Sizer (nano-SMPS). Nano-SMPS has been used to obtain PSDFs of soot particles produced in a burner stabilized flat-flame (BSFF)

and well-stirred reactor/plug flow reactor (WSR/PFR) [60, 62]. Previous work in these flow configurations have provided foundational understanding on soot coagulation and growth mechanisms.

The study conducted by Zhao et al. [59–61] to obtain soot particle size distribution in BSFF used the probe sampling method with negligible particle losses in the probe and the sampling line. A critical dilution ratio of the order of $\sim 10^4$ was reported above which the absolute number concentration and mean diameter of soot PSDF remained almost same. It was found that the size spectra in the nucleation region follows a power law or exponential decay function. As the residence time increased, the PSDF evolved into a bimodal distribution which is characteristic of the simultaneous occurrence of particle nucleation and particle-particle coagulation.

Experiments conducted by Manzello et al. [62] in NIST used a WSR followed by PFR to study PAH growth and soot inception using the similar sampling procedure as described in [60] and used SMPS for online sampling. The results were consistent with the understanding that acetylene and other small aromatics are key species in the pathway to soot particle formation. The study also concluded that the qualitative trends of aromatic concentration agreed with the changes in soot concentration.

Sampling of the soot particles from the reacting flows such as BSFF or MFTR is not trivial and offers many major challenges [59, 60]. The small particles tend to diffuse to the wall of the probe or the sampling line. In addition, there are particle losses due to particle-particle coagulation [63–65]. To minimize these losses sufficient dilution with non-reacting gas like nitrogen is essential. The dilution also helps in quenching chemical reactions and therefore prevents growth of particles in the probe and sampling line.

One of the initial tasks undertaken in this work was to validate the probe diagnostic technique by reproducing the literature data [60] using a BSFF McKenna burner. The flat-flame burner was built with a cylindrical stainless steel sintered porous matrix with embedded tubes for a coolant. Around the matrix there is a porous stainless steel ring through which a nitrogen shroud co-flow eliminates the entrainment of surrounding cold air into the flame. The experimental set up was similar to the earlier work of Zhao et al. [60] in which they employed a stainless steel tube with a small orifice for sample intake. The results obtained using this experimental set up agreed well with the published work.

After establishing the capability of our system to reproduce soot PSDF in BSFF, similar probe sampling method was used to obtain soot PSDF in an atmospheric microflow tube reactor (MFTR). The MFTR setup is conceptually somewhat similar to the Princeton Turbulent Flow Reactor (PTFR) [66] except that the small scale of the present system helps in eliminating the uncertainties associated with mixing of the fuel and the inert carrier gas. Experiments were performed to collect soot PSDF for pyrolysis and oxidation of ethylene fuel for range of temperature, residence times and equivalence ratios.

1.4 Outline of Thesis

The organization of this thesis continues as follows:

Chapter 2 - Laboratory Experimental Set-Up

The general experimental set-up and description is presented here for BSFF and MFTR. The theory of operation of SMPS and its components is also discussed here. The flow rate through orifice of the sample probe is calibrated and validated at different temperatures.

Chapter 3 - Mathematical Model of PSDF

The numerical model, comprising gas phase submodel and aerosol discrete sectional submodel model, is described here in detail. The discrete sectional method has three modules: nucleation, coagulation and surface growth.

Chapter 4 - Results

The results obtained from experiments and sectional model are presented here. Soot PDFs are measured using probe sampling and SMPS for oxidation case in BSFF and for both oxidation and pyrolysis cases in MFTR. The experimental operating conditions are simulated in the model and the results are compared.

Chapter 5 - Conclusions

The conclusions drawn from the experiments and the model are summarized in this chapter. The course of future work is also briefly outlined.

Chapter 2

Laboratory Experimental Set-Up

The experiments were conducted in two phases. First phase was the validation of probe sampling method using a burner stabilised flat-flame (BSFF) by reproducing the soot PSDF data published in previous works [58, 60]. In the second phase the above probe sampling method was used to obtain soot PSDF for pyrolysis and oxidation cases in an atmospheric micro-flow tube reactor developed at UVA [67]. The online sampling was done using a nano-SMPS which is a TSI model consisting of a Classifier (model 3080), nano-Differential Mobility Analyzer (n-DMA model 3085) and a nano-Condensation Particle Counter (n-CPC model 3788). For best resolution and size range in the current experiments, the SMPS was set to dual-blower mode with the sheath flow rate of 6 *lpm* and the inlet sample flow rate of 1.5 *lpm* giving a particle size range of 3.5 – 102 *nm*.

2.1 Laboratory Set-UP of Reactors

2.1.1 Set-Up for Burner Stabilized Flat Flame

The experimental set up is schematically shown in Fig. 2.1. A laminar premixed flame of ethylene and air with an equivalence ratio (ϕ) of 2.1 is stabilized on the flat-flame McKenna burner. The McKenna burner was fabricated at UVA to simulate the probe design used in the experiments of Zhao et al. [60]. The burner had a cylindrical sintered bronze plug of diameter of 25 *mm* with embedded tubes for a coolant. The mixture of air and fuel is introduced in such a way that there is an even distribution throughout

the porous matrix. Around the matrix there is a porous ring of OD 42.5 mm , through which a nitrogen shroud co-flow can be introduced to eliminate secondary flames at the edges. The flame is stabilized with a stainless steel mesh plate of the same diameter as burner which is located 21 mm above the burner. The cold gas velocity of mixture (air and ethylene) was set 8 cm/s , similar to that reported in [60].

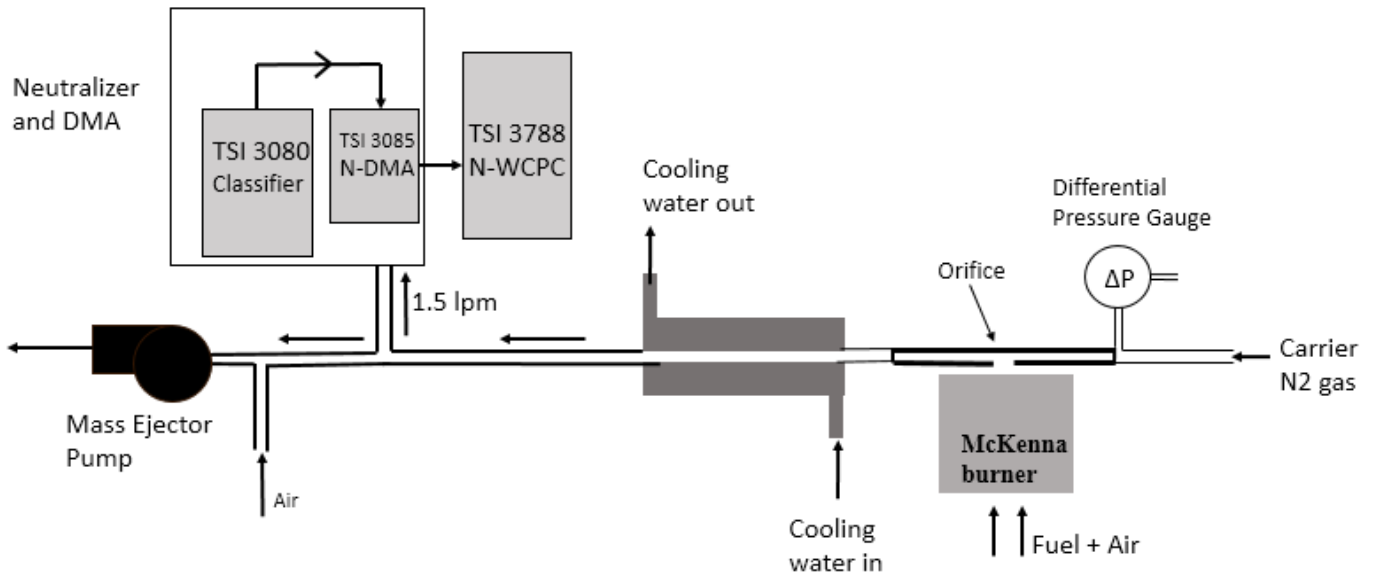


FIGURE 2.1: Schematic of experiment set-up for burner stabilized flat-flame

The sample probe was made of stainless steel cylindrical tube of OD $3/8\text{ in}$, 0.6 mm thickness and 20 cm length. A small rectangular groove was milled in the center of the tube of depth 0.5 mm to facilitate the drilling of orifice at its center. The diameter of the orifice was 0.13 mm and the thickness of the wall surrounding it was 0.1 mm .

The sampling probe with different orifice diameter and thickness were used in earlier studies [58, 62, 68] to obtain desirable dilution ratio between incoming hot gases and the inert carrier gas in the sampling probe. In the work by Zhao et al., the orifice diameter used was 0.2 mm with wall thickness of 0.7 mm to obtain dilution ratio of order 10^4 . In this work, different probes were used with orifice diameter varying from 0.25 mm to 0.13 mm and wall thickness varying from 0.1 mm to 0.6 mm . To obtain similar dilution ratios in this work, the orifice diameter in the probe was finally selected to be 0.13 mm due to small thickness of the wall surrounding the orifice.

The probe was fixed in a horizontal position with the orifice facing downwards directly opposite to the flame. A differential pressure gauge of range 0 to 250 Pa was connected upstream of the orifice to measure the suction pressure across the orifice in the sampling line. The probe was cooled by a copper cooling block inserted downstream on the probe. The temperature of the sample gases before SMPS inlet was measured to be 303 – 306 K and was always kept below 308 K . The incoming flow from the probe (downstream of water-jacket) was split into two parts with a small portion, of 1.5 lpm , was fed to the SMPS using silicone conductive tubes and the remaining portion was exhausted out through a pump connected downstream of the SMPS. An incoming flow of air is connected downstream of the SMPS to get precise control over the suction pressure in the sampling probe.

The flame gases containing soot particles were drawn in the orifice due to a small suction pressure across the orifice. As soon as the gases entered the probe, they were rapidly mixed and cooled down by the carrier nitrogen gas with a flow rate of 42 lpm . This rapid mixing ensured a dilution ratio in the vicinity of 1.6×10^4 to 1.7×10^4 . The cooling down of hot flame gases also quenched chemical reaction on the surface of soot particles [60].

2.1.2 Set-up for Micro-flow Tube Reactor (MFTR)

The schematic of micro-flow tube reactor and the sampling set-up are shown in Fig. 2.2. It is made up of a quartz tube of internal diameter 4 mm surrounded by modular heaters. The main flow (98% nitrogen in these experiments) is preheated to the target temperature (1200 K) in a 60 cm long helical section. The fuel (ethylene in this case) is introduced via two opposed quartz tubing of 1 mm ID just downstream of the helical section. Immediately downstream of the junction, a porous quartz frit is installed to facilitate rapid mixing of the fuel and the main flow of diluent nitrogen. The mixing results were verified by species mole fraction measurements prior to attaching the hot section.

The hot section which extends from the frit to the tube exit plane (Fig. 2.2) is 37 cm long and is maintained at the target temperature using six PID controllers connected to K-type thermocouples placed adjacent to the outside wall of the tube. The temperature

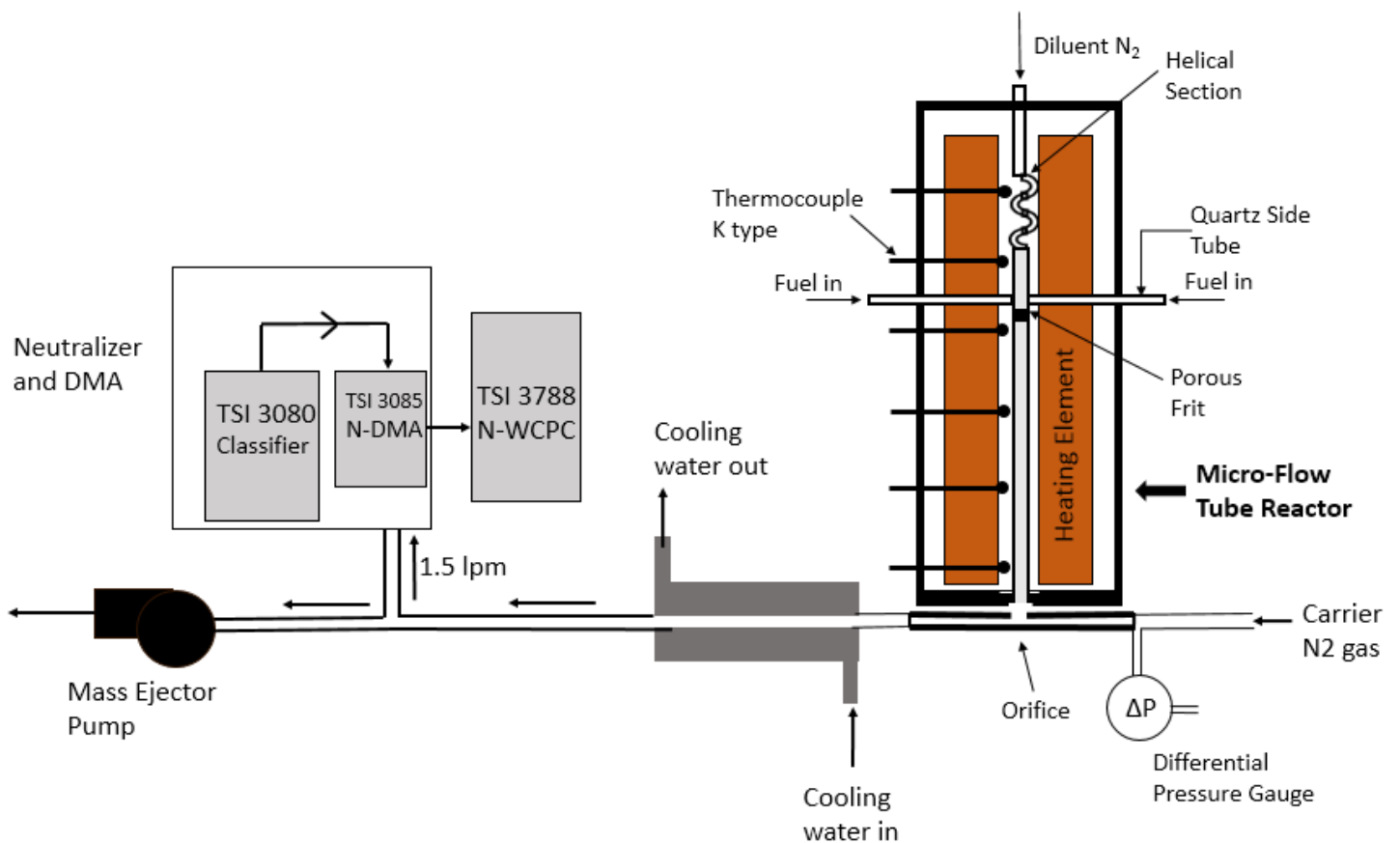


FIGURE 2.2: Schematic of experiment set-up for micro-flow atmospheric tube reactor (MFTR)

was measured inside and outside of the tube showed a variation of 5 K , with endothermic pyrolysis cases showing a slight drop in temperature while exothermic oxidation cases showing slight increase.

The sampling probe was installed in horizontal position at the exit of the tube reactor (Fig. 2.2). The configuration was similar to the one described above for the case of BSFF. The probe was made of stainless steel cylindrical tube of OD $3/8\text{ in}$, 0.65 mm thickness and 30 cm length. A small rectangular groove was milled in the center of the tube of depth 0.5 mm to facilitate the drilling of orifice at its center. The diameter of the orifice was 0.25 mm and the thickness of the wall surrounding it was 0.15 mm .

The flow rate through the orifice was calibrated for atmospheric air as described in Section 2.3 for different temperatures. A differential pressure gauge of range 0 to 250 Pa was connected upstream of the orifice to measure the suction pressure across the orifice

in the sampling line. The probe was cooled by a copper cooling block inserted downstream on the probe. The incoming flow from the probe (downstream of cooling block) was split into two parts with a small portion of 1.5 *lpm* was fed to the SMPS using silicone conductive tubes and the remaining portion was exhausted out through a pump connected downstream of the SMPS.

The hot gases at the exit of MFTR containing soot particles were drawn in the orifice due to a small suction pressure across the orifice. As soon as the gases entered the probe, they were rapidly mixed and cooled down by the carrier nitrogen gas. The flow rate of the nitrogen gas (10 *lpm* to 40 *lpm*) and the differential pressure (25 to 200 *Pa*) across the orifice were varied depending on the residence time inside the MFTR resulting in dilution ratio in the range of 0.6×10^3 to 7×10^3 .

2.2 Scanning Mobility Particle Sizer

SMPS is a high resolution nanoparticle sizer which allows real time online sizing of soot particles obtained from different flow conditions. The nano-SMPS used in this work is a TSI model consisting of a Classifier, nano-Differential Mobility Analyzer and a nano-Condensation Particle Counter. The aerosol particles first enters the Classifier through an Impactor. Inside the Classifier the aerosol particles are charged. These charged particles are selected using electrical classification (electrical mobility) inside n-DMA. The selected particles are counted in the n-CPC.

A small sample of flow rate 1.5 *lpm* is fed to the n-SMPS through an Inertial Impactor [2] which removes particles above a known particle size by accelerating the flow through a 0.071 *cm* nozzle directed at a flat plate (Fig. 2.3). The aerodynamic particle size [69] at which the particles are separated is called the cut-point diameter (D_{50}) and is given by

$$D_{50} = \sqrt{\frac{9\pi St\mu W^3}{4\rho_s CQ}} \quad (2.1)$$

where; D_{50} is the particle cut-point diameter (*cm*, 50% cut efficiency), St is the Stokes number(0.23), ρ_s is the particle density (*g/cm³*), Q is the volumetric flow rate (*cm³/s*),

D_p is the particle diameter (cm), μ is gas viscosity (dynes/cm^2), W is the nozzle diameter (cm) and C is the Cunningham Slip Correction factor given by,

$$C = 1 + Kn[\alpha + \beta \exp(-\gamma/Kn)] \quad (2.2)$$

here; $\alpha = 1.142$, $\beta = 0.558$, $\gamma = 0.999$, Kn is the Knudsen number: $Kn = 2\lambda/D_p$ and λ is the gas mean free path

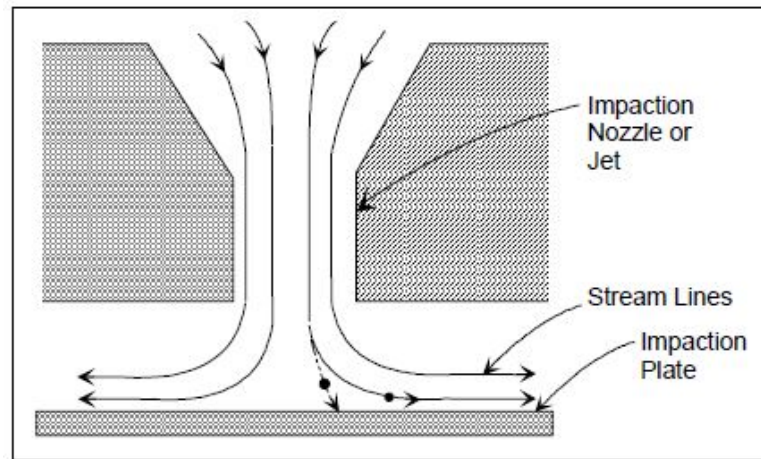


FIGURE 2.3: Cross-Sectional view of Inertial Impactor [2]

In the Electrostatic Classifier, the particles enter a Kr-85 Bipolar Charger (or neutralizer) which exposes the aerosol particles to high concentrations of bipolar ions. The particles and ions undergo frequent collisions due to the random thermal motion of the ions. The particles quickly reach a state of charge equilibrium, in which the particles carry a known bipolar charge distribution. The charged soot particles pass from the neutralizer into the main portion of the Differential Mobility Analyzer (DMA), shown in Fig. 2.4. The DMA contains two concentric metal cylinders. The polydisperse particles and sheath air are introduced at the top of the Classifier and flow down the annular space between the cylinders. The particle flow surrounds the inner core of sheath air, and both flows pass down the annulus with no mixing of the two laminar streams. The inner cylinder, the collector rod, is maintained at a controlled negative voltage, while the outer cylinder is electrically grounded. This creates an electric field between the two cylinders. The electric field causes positively charged particles to be attracted through the sheath air to the negatively charged collector rod. Particles are precipitated along the length of the collector rod.

The location of the precipitating particles depends on the the Classifier flow rates, the Classifier geometry and the particle electrical mobility (Z) given by Eq. 2.3 [69, 70]. Particles with a high electrical mobility are precipitated along the upper portion of the rod; particles with a low electrical mobility are collected on the lower portion of the rod. Particles within a narrow range of electrical mobility exit with the monodisperse air flow through a small slit located at the bottom of the collector rod. These particles are transferred to a particle sensor to determine the particle concentration. The remaining particles are removed from the Classifier via the excess air flow.

$$Z = \frac{n\epsilon C}{3\pi\mu D_p^{mobility}} \quad (2.3)$$

where; n is the number of elementary charges on the particle, e is the elementary charge ($1.6 \times 10^{-19} \text{Coulomb}$) and $D_p^{mobility}$ is the diameter of the particle measured by SMPS(cm).

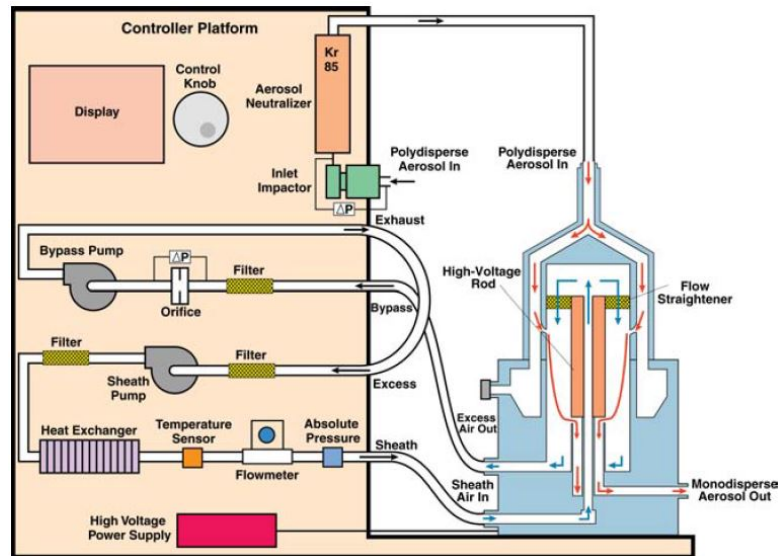


FIGURE 2.4: Flow schematic for the Electrostatic Classifier with nano-DMA in dual-blower mode [3]

The mono-disperse particles exiting the DMA enters the nano-Water Condensation Particle Counter (n-WCPC) where the particles are enlarged by a condensing vapor to form easily detectable droplets. The vapor surrounding the particles reaches a certain degree of supersaturation and begins to condense onto the particles. The degree of supersaturation is measured as the supersaturation ratio (P/P_s), which is defined as the actual vapor partial-pressure divided by the saturation vapor pressure for a given temperature.

For a given saturation ratio, the vapor can condense onto particles only if they are big enough. The minimum particle size capable of acting as a condensation nucleus is called the *Kelvin diameter* [71, 72]

$$\frac{P}{P_s} = \exp\left(\frac{4\gamma M}{\rho_c R T d_{Kelvin}}\right) \quad (2.4)$$

where; γ is the surface tension of the condensing fluid, M is the molecular weight of the condensing fluid, ρ_c is the density of the condensing fluid, T is the absolute temperature, d_{Kelvin} is the *Kelvin diameter*.

The sensor inside the n-WCPC contains a conditioner, a growth tube, and an optical detector (Fig. 2.5). The sample flow is cooled with a thermo-electric device in the conditioner. The vapor passes into the growth tube where it becomes supersaturated and condenses onto the particles to form large droplets. The large droplets are detected by the optical detector which uses a laser diode. The current model of n-WCPC counts single particles with continuous, live-time coincidence correction up to 4×10^5 particles/cm³.

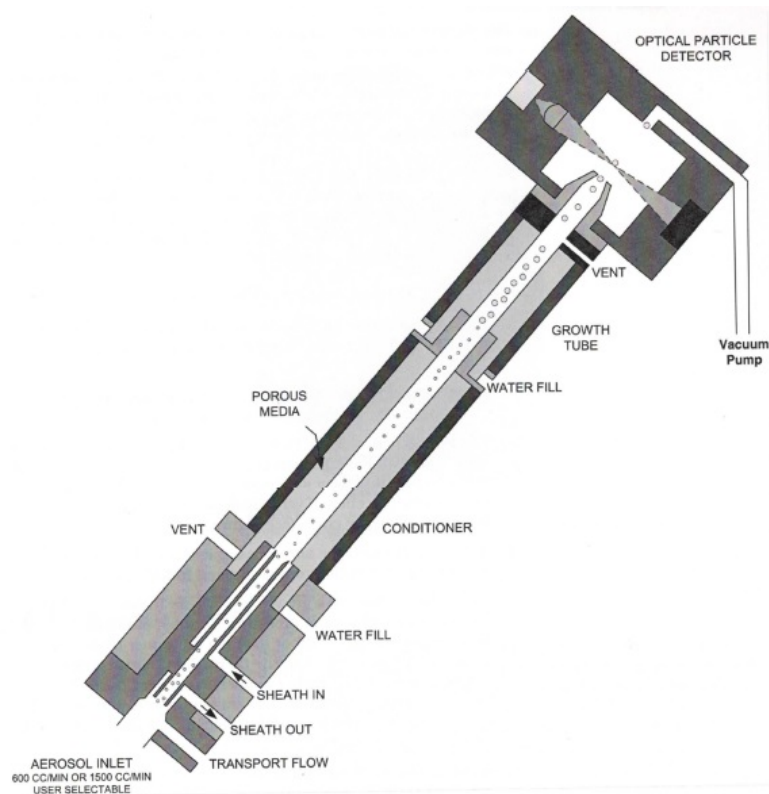


FIGURE 2.5: Flow schematic for the nano-CPC [4]

In the present study the setting of SMPS was set to allow an inlet sample flow rate of 1.5 *lpm* and sheath flow rate of 6 *lpm* in a dual blower mode which helped in reducing transport time and, therefore, diffusive particle losses. The n-CPC in these setting has lower size limit of 3 *nm*. Typically a particle size spectrum was obtained from a 120s up-scan and a 15s down-scan.

2.2.1 Mobility Diameter

Mobility diameter is the particle diameter measured by SMPS which is based on the electrical mobility in the zero strength limit [73]. The technique used in SMPS to calculate the electrical mobility employs empirical Stokes-Cunningham formula given by Eq. 2.3 [69, 70].

In the studies conducted by Li et al. [74, 75] and others [61], it was found that Eq. 2.3 is limited in its accuracy for nano-sized particles. It was proposed [75] that for an ideal gas with $Kn \ll 1$, the particle mobility be modeled as

$$Z = \frac{3}{2} \sqrt{\frac{kT}{2\pi m_r}} \frac{pne}{D_p^2 \Omega_{avg}^{(1,1)*}} \quad (2.5)$$

where; k is the Boltzmann constant, T is the temperature, m_r is the reduced mass, p is pressure, D_p is the proposed true particle diameter and $\Omega_{avg}^{(1,1)*}$ is the average reduced collision integral given by Li et al. [75].

The relationship between the mobility diameter ($D_p^{mobility}$) and the true diameter (D_p) is obtained from equating Eq. 2.3 and 2.5 and is plotted in Fig. 2.6. The particle diameter measured by SMPS is corrected based on this fit (Fig. 2.6) in all the measured results presented in this work.

2.3 Calibration of Orifice Flow Rate

As the hot flame gases are drawn into the probe, they are diluted by a carrier gas (cold nitrogen in this case). The dilution ratio between the incoming hot gases and the carrier nitrogen gas is obtained by calculating the volumetric flow rate of flame gases

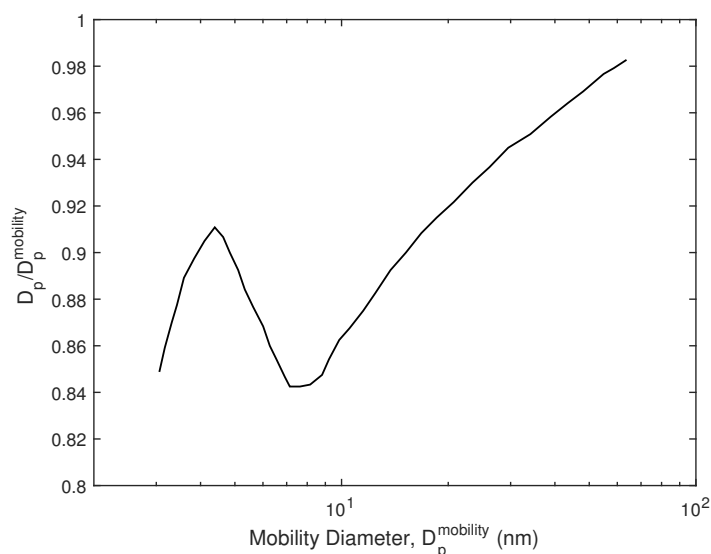


FIGURE 2.6: Relation between particle diameter and the mobility diameter

through the orifice. The volumetric flow rate of carrier gas nitrogen (Q_c) for experiments on BSFF was kept constant at 42 lpm . The flow rate through the orifice is calibrated by plugging one end of the probe and connecting its other end to a pump through a flow meter in purge mode. A pressure transducer is connected upstream of the orifice. Atmospheric air at different temperatures is used to calibrate the probe orifice. The observed volumetric flow rate versus differential pressure across orifice for a probe with $250 \mu\text{m}$ orifice is plotted in Fig. 2.7.

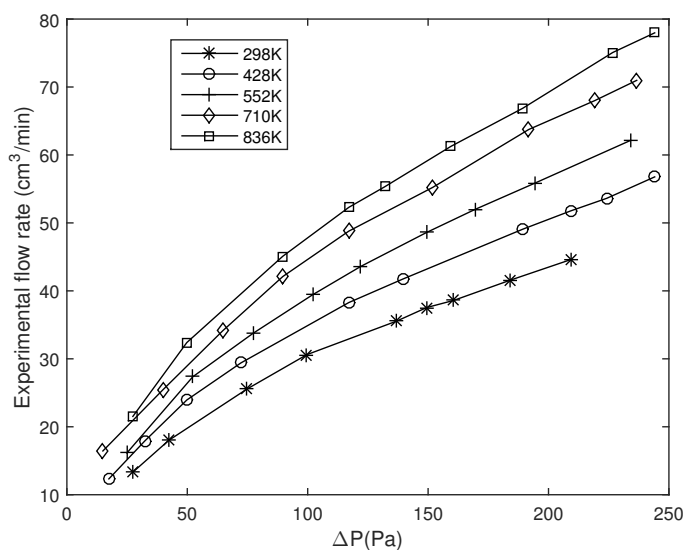


FIGURE 2.7: Experimental Flow rate through orifice versus differential pressure across orifice for $250 \mu\text{m}$ orifice

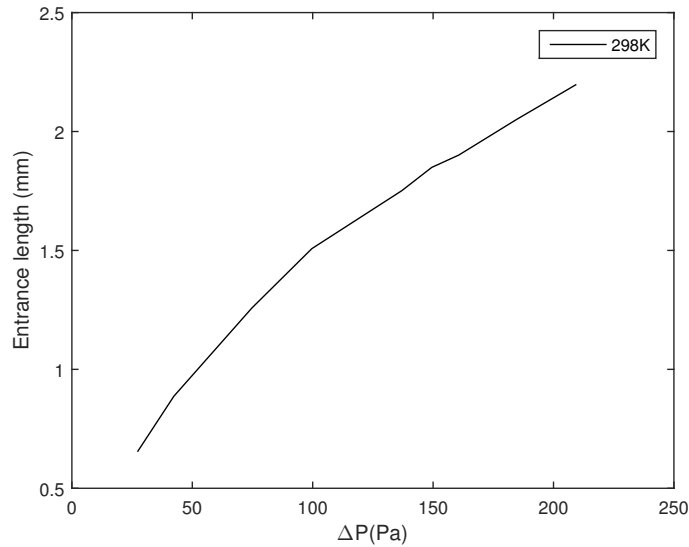


FIGURE 2.8: Variation of entrance length of flow through $250 \mu\text{m}$ orifice with variation in pressure across orifice

The flow through the orifice is not fully developed as the orifice diameter ($250 \mu\text{m}$) is comparable to the thickness of the wall surrounding the orifice ($150 \mu\text{m}$). The entrance length of the flow with variation in suction pressure is calculated at temperature 298K and plotted in Fig. 2.8. Clearly, the entrance length is larger than the thickness of the wall and therefore the flow is still developing. This is in contrast with the published work of Zhao et al. [60] in which case the flow was considered as fully developed. One of the reasons for this difference can be the thickness of the wall surrounding the orifice which in the case of Zhao et al. [60] was 0.7 mm .

$$Q_o = A \left(c_1 \frac{\Delta P}{T^{0.8}} + c_2 T^{1/2} \Delta P^{1/2} \right) \quad (2.6)$$

where, c_1 and c_2 are the calibration constant found to be 0.8 and 0.054 for the orifice diameter of $250 \mu\text{m}$ and 1.7 and 0.065 for the orifice diameter $130 \mu\text{m}$ respectively and A is the cross sectional area of orifice.

Our calibration showed that flow velocity through orifice (and therefore, flow rate(Q_o)) is only the function of temperature and differential pressure across orifice as given by Eq. 2.6. The first term in RHS is the dependence of velocity on gas viscosity and collision cross-section. The second term is due to the Bernoulli's equation for developing flow.

The experimental flow rate and the calibrated flow rate through the orifice for the cases of $250\ \mu\text{m}$ and $130\ \mu\text{m}$ orifices are presented in Fig. 2.9 and Fig. 2.10 respectively. The experimental flow rate agrees well with the calibrated flow rate.

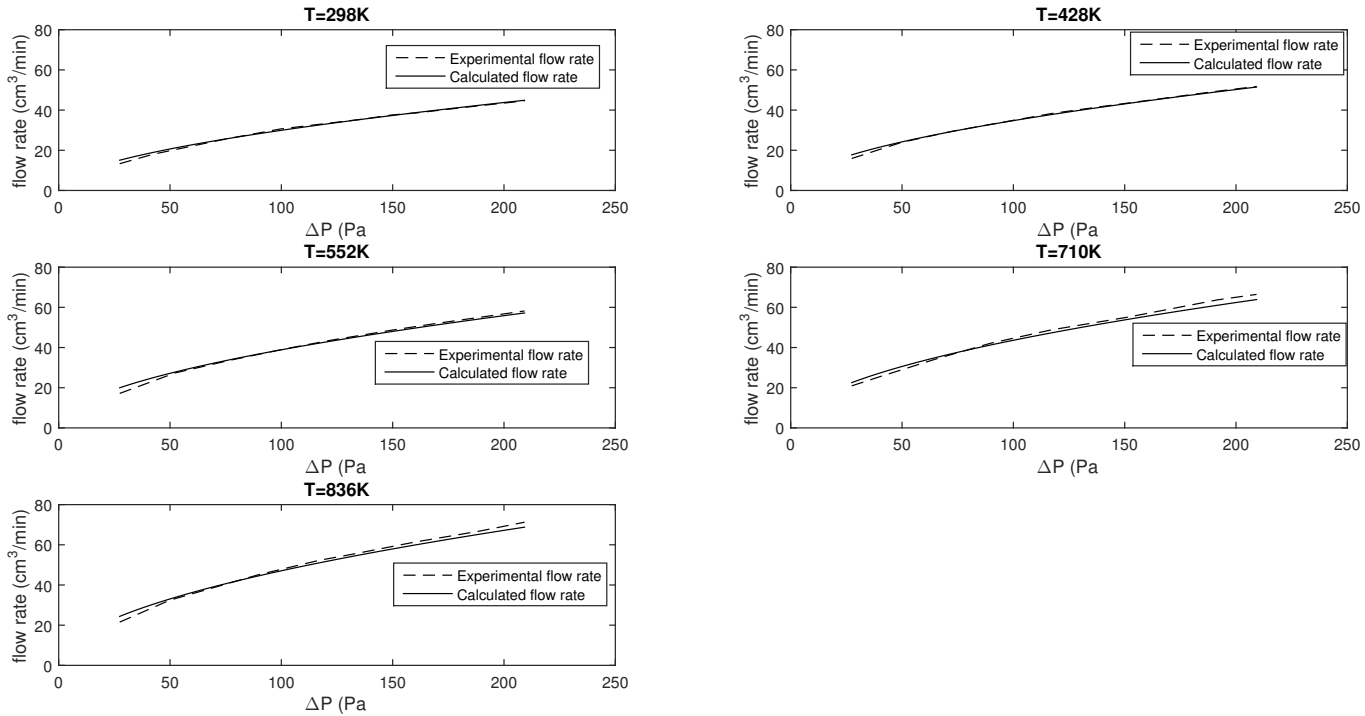


FIGURE 2.9: Comparison of experimental flow rate and calculated flow rate through orifice as a function of differential pressure across orifice for $250\ \mu\text{m}$ diameter for different temperatures

2.4 Summary

The detailed experimental set-up including the probe sampling, the McKenna burner and the atmospheric MFTR was described in this chapter. The theory of operation of particle sizer (SMPS) used in this study to measure soot particles was also described in this chapter. It was reported in earlier studies that mobility diameter measured by SMPS is limited in its accuracy for nano-sized particles and was, therefore, corrected to improve the accuracy. The flow rate through the sampling probe orifice was calibrated for both $250\ \mu\text{m}$ and $130\ \mu\text{m}$ orifice diameters. The orifice flow rate was used to calculate the dilution ratio between the carrier nitrogen gas and the incoming hot gases through orifice as described in chapter 4.

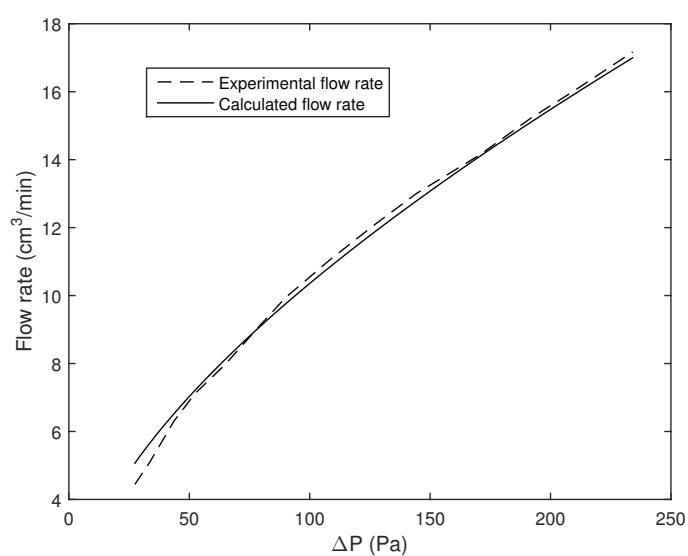


FIGURE 2.10: Comparison of experimental flow rate and calculated flow rate through orifice as a function of differential pressure across orifice for $130\ \mu\text{m}$ diameter at $298\ \text{K}$

Chapter 3

Mathematical Model of PSDF

A numerical FORTRAN model was developed to model soot nucleation and growth for a homogeneous reacting gas mixture in a zero dimensional constant volume closed system [76]. The model runs in conjunction with the Chemkin software package which provides information on equations of state, thermodynamic properties, and chemical production rates of the species specified in an input reaction-mechanism file. The model developed can be divided into two submodels: (1) gas phase reaction submodel which provides the species concentration profile [77] and (2) particle dynamics submodel which determines the soot particle nucleation and the surface growth rates. At each time step, the concentrations of gas phase species are calculated based on their production or depletion in the gas phase chemical reactions as well as their consumption in the formation of soot particles, given by

$$\frac{dY_k}{dt} = \left(\frac{dY_k}{dt} \right)_{gas} + \left(\frac{dY_k}{dt} \right)_{soot}, \quad k = 1, \dots, N_{sp} \quad (3.1)$$

where, Y_k is the mass fraction of k_{th} species and N_{sp} is the total number of the species.

In this chapter, the equations used to obtain gas phase reactions rates are described in section 3.1. Section 3.2 describes in detail the sectional aerosol model for soot particles. The sectional model has three modules which include particle nucleation, particle-particle coagulation and particle surface growth. The final section 3.3 describes the coupling of gas-phase and particle dynamics submodels.

3.1 Gas Phase Reaction Model

For highly diluted cases considered, the reacting mixture in a fluid element is a closed system with no mass crossing the boundary so that the total mass of the mixture,

$$m = \sum_{k=1}^{N_{sp}} m_k \quad (3.2)$$

is constant. Here, m_k is the mass of the k_{th} species and N_{sp} is the total number of species. The individual species are produced or destroyed according to

$$\left(\frac{dm_k}{dt} \right)_{gas} = V \dot{\omega}_k W_k \quad (3.3)$$

where, t is time, V is the constant volume of the system, $\dot{\omega}_k$ is the molar production or depletion rate of the k_{th} species due to gas-phase reactions and W_k is the molecular weight of the k_{th} species.

Alternatively, Eq. 3.3 can also be written in terms of mass fraction as the total mass is constant.

$$\left(\frac{dY_k}{dt} \right)_{gas} = \frac{1}{\rho_{sp}} \dot{\omega}_k W_k \quad (3.4)$$

where, $Y_k = \frac{m_k}{m}$ is the mass fraction of the k_{th} species, and ρ_{sp} is the density of species.

The net production or depletion rate, $\dot{\omega}_k$, of a species results from the competition between all the chemical reactions which involve that species (including the reactions of the species in the particle growth model as described in Eq. 3.1). The forward rate constant (k_f) of a reaction k is evaluated using the modified Arrhenius equation.

$$k_f = A_k T^{\beta_k} \exp\left(\frac{-E_k}{RT}\right), \quad k = 1, \dots, N_r \quad (3.5)$$

where, T is the temperature, R is the universal gas constant, E_k is the activation energy of the k_{th} reaction, A_k is the pre-exponential constant of the k_{th} reaction, β_k is the temperature exponent of the k_{th} reaction and N_r is the total number of reactions.

The Arrhenius constants and the activation energy of the relevant reactions used in this model are obtained from reaction mechanism input file proposed by Slavinskaya

et al. [77]. The relevant CHEMKIN subroutines are called from the model to obtain these parameters. At each time step the reaction rates due to gas-phase chemistry and particle growth are fed to a stiff ODE solver in Fortran which in the present work is the open-source SUNDIALS CVODE Solver [78, 79].

In the present model, pyrene ($C_{16}H_{10}$) is considered as the only PAH species contributing to soot nucleation[21, 80] where two pyrene molecules combine together to form a single soot particle.

3.2 Particle Nucleation and Growth Model

The soot aerosol particles undergo simultaneous nucleation, coagulation and surface growth governed by following population balance equation (*PBE*) [46]:

$$\frac{\partial n(v, t)}{\partial t} = \frac{1}{2} \int_0^v \beta(v-v', v') N(v-v', t) N(v', t) dv' - N(v, t) \int_0^\infty \beta(v, v') N(v', t) dv' + S(v) + G(v) \quad (3.6)$$

where, v, v' are the volumes of the interacting particles, $N(v, t)$ is the particle size distribution function at time t , $\beta(v, v')$ is the collision coefficient of two particles of volume v and v' , $S(v)$ is the nucleation term of particle of volume v and $G(v)$ is the growth term of particle of volume v

The PBE Eq. 3.6 is solved numerically as proposed by Kumar and Ramakrishna [46] by discretization using a fixed pivot technique. In this method the entire particle size range is divided into small sections (bins) where particles in each bin are represented by a constant size (volume in this model). In Eq. 3.6, the LHS represents the change in number concentration of particles in a specific bin i .

In the current fixed sectional bin model, entire particle size (volume) is divided into a number of volume bins by a geometric series as

$$v_k = v_0 f_v^{k-1}, \quad k = 1, \dots, N_{bins} \quad (3.7)$$

where, v_k is the volume (cm^3) of the k^{th} bin, v_0 is the lowest volume (cm^3) of particle size distribution (which is equal to the volume of two pyrene molecules in this model), f_v is the ratio of volumes of two consecutive bins ($f_v = 2.0$ used in this model).

All the soot particles are forced to have the same volume as one of these representative bin volumes. The maximum number of bins, N_{bins} , can be determined using the user input variables v_0 , f_v and biggest volume bin, v_{max} (cm^3) as

$$N_{bins} = \frac{\log(v_{max}/v_0)}{\log(f_v)} + 1 \quad (3.8)$$

The rate of change of particle number concentration in a bin k is due to coagulation, surface growth and nucleation:

$$\frac{dN_k}{dt} = \left(\frac{dN_k}{dt}\right)_{nucl} + \left(\frac{dN_k}{dt}\right)_{coag} + \left(\frac{dN_k}{dt}\right)_{gr}, \quad k = 1, \dots, N_{bins} \quad (3.9)$$

where, N_k is the particle number concentration in a bin k and the subscripts *nucl*, *gr* and *coag* stand for nucleation, growth and coagulation respectively.

3.2.1 Collision Frequency Coefficient

The collision frequency coefficient [47], $\beta_{i,j}$, (cm^3/s) which is the rate at which the two particles of i^{th} and j^{th} volume size collide is given by Eq. 3.10. This coefficient is used to calculate the rate of particle nucleation, particle coagulation and particle surface growth.

$$\beta_{i,j} = 2\pi(D_i + D_j)(d_i + d_j) \left(\frac{d_i + d_j}{d_i + d_j + 2(g_i^2 + g_j^2)^{1/2}} + \frac{8(D_i + D_j)}{(\bar{c}_i^2 + \bar{c}_j^2)^{1/2}(d_i + d_j)} \right)^{-1} \quad (3.10)$$

$$\bar{c}_i = \left(\frac{8kT}{\pi m_i} \right)^{1/2} \quad (3.11)$$

$$l_i = \frac{8D_i}{\pi \bar{c}_i} \quad (3.12)$$

$$g_i = \frac{1}{3d_i l_i} \left((d_i + l_i)^3 - (d_i^2 + l_i^2)^{2/3} \right) - d_i \quad (3.13)$$

$$Kn_i = \frac{2\lambda_{gas}}{d_i} \quad (3.14)$$

$$C_{c,i} = \frac{5 + 4Kn_i + 6Kn_i^2 + 18Kn_i^3}{5 - Kn_i + (8 + \pi) + Kn_i^2} \quad (3.15)$$

$$D_i = \frac{kTC_{c,i}}{3\pi\mu d_i} \quad (3.16)$$

where, $C_{c,i}$ is Cunningham slip correcting factor [dimensionless], \bar{c}_i is thermal velocity of a particle in i^{th} bin (cm/s), D_i is diffusion coefficient of a particle in i^{th} bin (cm^2/s), d_i is diameter of a particle in i^{th} bin (cm), g_i is a characteristic length of a particle in i^{th} bin (cm), k is Boltzmann constant (erg/K) [1.38054×10^{16} erg/K], Kn_i is Knudsen number of a particle in i^{th} bin (dimensionless), l_i is mean free path of a particle in i^{th} bin (cm), m_i is mass of a particle in i^{th} bin or (g), T is temperature (K), $\beta_{i,j}$ is the coagulation coefficient between a particle in i^{th} bin and a particle in j^{th} bin (cm^3/s), λ_{gas} is mean free path of gas (cm) and μ_{gas} is gas viscosity (g/cm-s).

3.2.2 Nucleation

The soot nucleation is the process of gas to particle formation where high molecular weight poly aromatic hydrocarbons (PAHs) molecules such as pyrene ($C_{16}H_{10}$) or PAH molecules bigger than pyrene collide with each other rendering some of the them to stick together. The newly formed particle or nucleus then grows by surface growth and coagulation. In this work, only pyrene contributed to the nucleation of soot particles. The nucleation rate is the rate of change in the number concentration in the first bin as Nucleation affects only the particle concentration in the first bin ($\#/cm^3 - s$), given by,

$$\left(\frac{dN_1}{dt} \right)_{nucl} = \beta \alpha_{nucl} [pyrene]^2 Av^2 \quad (3.17)$$

where, $[pyrene]$ is the molar concentration of pyrene, Av is the Avogadro number, β is the collision frequency coefficient for the collision between two pyrene molecules and is obtained using Eq. 3.10 in Section 3.2.1 and α_{nucl} is the collision efficiency in nucleation.

In the gas phase, the rate $(\frac{dY_{pyrene}}{dt})$ at which pyrene is depleted due to nucleation is:

$$\left(\frac{dY_{pyrene}}{dt}\right)_{nucl} = -2(\beta), \alpha_{nucl} [pyrene]^2 Av \quad (3.18)$$

3.2.3 Coagulation

The newly formed particles collide randomly with each other and some of them stick to form larger particles. These larger particles undergo further collision to coagulate with particles of different sizes. This process continues so that the mode of particles size distribution shift towards larger sizes. Due to coagulation total soot number concentration ($\#/cm^3$) decreases but the total soot mass concentration (g/cm^3) remains unchanged.

The rate of change of particle concentration in bin i due to coagulation is [46],

$$\left(\frac{dN_i}{dt}\right)_{coag} = \sum_{\substack{k \leq j \leq i \\ v_{i-1} \leq v_j + v_k \leq v_{i+1}}} (1 - \frac{\delta_{j,k}}{2}) \eta_{j,k} \beta_{j,k} \alpha_{coag} N_j N_k - N_i \sum_{k=1}^{N_{bins}} \beta_{i,k} \alpha_{coag} N_k \quad (3.19)$$

where, $\beta_{j,k}$ is the collision frequency coefficient for coagulation between particles of bins j and k and is obtained using Eq. 3.10 in Section 3.2.1, α_{coag} is the collision efficiency for coagulation, $\delta_{j,k}$ is the Kronecker delta function and N_i is the number concentration in bin i .

The first term in RHS of Eq. 3.19 represents the addition of new particles in bin i due to coagulation of particles from smaller bin sizes. The second term in RHS represents the loss of particles from bin i due to coagulation of particles from bin i with particles from other bin sizes. The process of particle-particle coagulation can result into new particles whose sizes do not match any of the representative bin sizes. To accommodate these particles, this method proposes to distribute these particles between the neighboring bins while conserving total mass and number of these particles [46, 81].

Hence, as soon as new particle is formed due to coagulation between particle from bins j and k , whose size (volume) is between two neighboring volume bins (v_{i+1} and v_i), it is distributed between these two neighboring volume bins (v_{i+1} and v_i) conserving their number and mass (volume) by the discrete sectional coagulation model. The partition coefficient used ($\eta_{j,k}$) [46] is defined as:

$$\eta_{j,k} = \left\{ \begin{array}{ll} \frac{v_{i+1} - (v_j + v_k)}{v_{i+1} - v_i} & v_i \leq v_j + v_k \leq v_{i+1} \\ \frac{(v_j + v_k) - v_{i-1}}{v_i - v_{i-1}} & v_{i-1} \leq v_j + v_k \leq v_i \end{array} \right\} \quad (3.20)$$

where, $\eta_{j,k}$ is the factor that preserves the mass and the number of the new particles by distributing them in the adjoining bins and v_i is the volume of particle representing bin i .

3.2.4 Surface Growth

The size of the soot particles also changes due to physical and chemical reactions on their surface. This growth changes the particle size distribution but does not affect the total number concentration of the particles. The surface growth mechanisms include 1) HACA mechanism [20, 47] presented in Table 3.1 in which carbon mass is accumulated on soot surface due to repeated reactions with acetylene (C_2H_2) gas, 2) soot oxidation by O_2 and OH (negative growth) (also presented in Table 3.1) where carbon mass is lost from soot surface and 3) PAH condensation where PAH gas molecules condense and accumulate on the soot surface [28, 32, 82].

3.2.4.1 HACA Mechanism and Oxidation

A dominant reaction pattern in the growth of an aromatic ring is H_2 abstraction and C_2H_2 addition (HACA). The reactions (1-5) in the table below (Table 3.1) represents the dominant reaction scheme for HACA mechanism. The reactions (6) and (7) provides the reaction path for soot oxidation by O_2 and OH .

TABLE 3.1: Soot Surface Growth Mechanism

$k = A_{Arr} T^{\beta_{Arr}} \exp(-E_{act}/RT)$					
Number	Reactions	A_{Arr}	β_{Arr}	E_{act}	Reference
1	$C_{soot} - H + H \longrightarrow C_{soot} \bullet + H_2$	4.2×10^{13}		13.0	[21]
2	$C_{soot} \bullet + H_2 \longrightarrow C_{soot} - H + H$	4.0×10^{11}	0	7.0	[21]
3	$C_{soot} - H + OH \rightleftharpoons C_{soot} \bullet + H_2O$	1.0×10^{10}	0.734	1.43	[21]
4	$C_{soot} \bullet + H \longrightarrow C_{soot} - H$	2.0×10^{13}			[21]
5	$C_{soot} \bullet + C_2H_2 \longrightarrow C_{soot} - H + H$	8.0×10^7	1.56	3.8	[21]
6	$C_{soot} \bullet + O_2 \longrightarrow 2CO + C_{soot}$	2.2×10^{12}	0	7.5	[21]
7	$C_{soot} - H + OH \longrightarrow C_{soot} + CO + H$	4.4×10^2	0.5		[21]

The seven reactions presented in Table 3.1 are used in the present model to simulate the surface growth on the surface of a soot particle. The reaction constant for each reaction is calculated using Arrhenius equation given by Eq. 3.5. The number of sites on the soot surface available (saturated sites) to undergo reaction is assumed to be a constant number of $2.3 \times 10^{15} \text{ sites/cm}^2$ [22]. The concentration of saturated sites ($C_{soot} - H$) in a bin i is calculated as

$$[C_{soot} - H]_i = 2.3 \times 10^{15} (SA)_i N_i \frac{1}{Av} \quad (3.21)$$

where, $[C_{soot} - H]_i$ is the molar concentration of saturated sites in the section bin i (mol/cm^3) and $(SA)_i$ is the representative surface area of the bin i (cm^2).

The concentration of unsaturated sites ($C_{soot} \bullet$) is calculated under the assumption that the saturated and the unsaturated sites are in equilibrium in a bin i and is obtained from the reactions presented in Table 3.1:

$$[C_{soot} \bullet]_i = \left(\frac{k_{1f}[H] + k_{3f}[OH]}{k_{2f}[H_2] + k_{3b}[H_2O] + k_{4f}[H] + k_{5f}[C_2H_2] + k_{6f}[O_2]} \right) [C_{soot} - H]_i \quad (3.22)$$

where, $[C_{soot\bullet}]_i$ is the molar concentration of dehydrogenated sites in the sectional bin i (mol/cm^3), k_{1f}, \dots, k_{7f} represent the forward reaction rate constant of the corresponding reactions presented in Table 3.1, k_{1b}, \dots, k_{7b} represent the backward reaction rate constant of the corresponding reactions, $[C_{soot-H}]_i$ is the molar concentration of saturated sites in the section bin i (mol/cm^3) and $[O_2], \dots, [H_2]$ are the molar concentrations of corresponding gas species O_2, \dots, H_2 (mol/cm^3).

Using the concentrations of saturated and unsaturated sites (Eqs. 3.21 and 3.22), the rate of change in the total mass of the particle $\left(\left(\frac{dm_i}{dt}\right)_{chem}, (g/s)\right)$ in a sectional bin i due to surface growth by chemical reactions is given by :

$$\left(\frac{dm_i}{dt}\right)_{chem} = \frac{(2 m_C k_{5f} [C_2H_2][C_{soot\bullet}]_i - 2 m_C k_{6f} [O_2][C_{soot\bullet}]_i - m_C k_{7f} [OH][C_{soot-H}]_i)}{N_i/Av} \quad (3.23)$$

where, m_C is the mass of one atom of carbon (g) and m_i represents the total mass of the particles in sectional bin i (g).

The rate of change in concentration of the gas species ($O_2, H_2, CO_2, CO, H, C_2H_2, H_2O$ and OH) due to chemical reactions in Table 3.1 are updated in the gas phase model in the same time step.

3.2.4.2 PAH Condensation

The collision between PAHs and soot particles results in PAHs condensation on the particles resulting in change in the volume of the soot particles without changing the total number concentration. In the current model only the pyrene condensation on soot particles is considered. The collision frequency coefficient between particles of bin i and the pyrene molecules is obtained using Eq. 3.10 in Section 3.2.1.

Rate of change in the total mass of particles $\left(\left(\frac{dm_i}{dt}\right)_{cond}, (g/s)\right)$ in the sectional bin i due to condensation of pyrene gas on the soot particles is given by:

$$\left(\frac{dm_i}{dt}\right)_{cond} = \beta_i \alpha_{cond} [pyrene] M_{pyrene} \quad (3.24)$$

where, M_{pyrene} is the molecular mass of pyrene, β_i is the collision frequency coefficient between particles of bin i and the pyrene molecules and α_{cond} is the collision efficiency for condensation.

The rate, $\left(\frac{dn}{dt}\right)_{pyrene}$, at which pyrene is depleted due to condensation is:

$$\left(\frac{dn}{dt}\right)_{pyrene} = - \sum_{i=1}^{N_{bins}} \beta_i [pyrene] N_i \quad (3.25)$$

3.2.4.3 Implementation of Surface Growth

The surface growth due to surface reactions through HACA mechanism, soot oxidation and PAH condensation is solved numerically in the discretized size domain of soot particles similar to Section 3.2.3. The rate of change in mass of particles in bin i due to surface growth mechanisms is:

$$\left(\frac{dm_i}{dt}\right)_{gr} = \left(\frac{dm_i}{dt}\right)_{chem} + \left(\frac{dm_i}{dt}\right)_{cond} \quad (3.26)$$

where, $\left(\frac{dm_i}{dt}\right)_{chem}$ and $\left(\frac{dm_i}{dt}\right)_{cond}$ are given by Eqs. (3.23) and (3.24) respectively and $\left(\frac{dm_i}{dt}\right)_{gr}$ is the total rate (g/s) of surface growth for section i .

Due to surface reactions, the volume, v , of each soot particle in a sectional bin i either decreases ($v_{i-1} < v < v_i$) or increases ($v_i < v < v_{i+1}$). Since only the particles of certain sizes (v_i, v_{i+1}, v_{i+2} etc.) can represent the bins, the new grown particles in bin i are re-assigned to their neighboring bins while conserving their mass and number concentration. In this model a two-point fixed section method [81] for surface growth is implemented to distribute the grown particles to adjacent bins.

$$\left(\frac{dN_i}{dt}\right)_{gr} = \frac{I_{i-1}N_{i-1}}{v_i - v_{i-1}} - \frac{I_i N_i}{v_{i+1} - v_i} \quad (3.27)$$

where, $\left(\frac{dN_i}{dt}\right)_{gr}$ is the change in number concentration of bin i due to surface reactions and $I_i = \frac{dv_i}{dt}$, is the rate of change in particles volume in bin i due to surface growth, given by Eq. 3.26.

3.3 Implementation

The model has two types of input parameters which are set by user. First group of input parameters are constant input parameter which does not need any optimization and second group of input parameters are optimized input parameters which need be optimized against measured data and sensitivity analysis. In this work, the model parameters were optimized to reproduce literature data [7]. Future modification may make this optimized input parameters as fixed input parameters or a function. The input parameters are given in Table 3.2 whose details are given in previous sections .

TABLE 3.2: Input variables of the model

No	Input variables	Is optimization required ?	Reference
1	Volume of smallest bin, v_0 is volume of a pyrene molecule (cm^3)	No	
2	Volume of biggest bin, v_{max} , is Volume of 1000 nm particle (cm^3)	No	
3	Ratio of 2 consecutive bin-volume, $f_v = 2.0$	No	
4	Nucleating PAH pair: Pyrene-Pyrene	Yes	[21]
5	Condensing PAH: Pyrene	Yes	[21]
6	Collision efficiency in nucleation, $\alpha_{nucl} = 0.001$	Yes	[32]
7	Collision efficiency in PAH-condensation, $\alpha_{cond} = 0.1$	Yes	
8	Collision efficiency in coagulation, $\alpha_{coag} = 1$	Yes	

The rate of change in number concentration of soot particles in each bin is contributed by Nucleation, Coagulation and Surface Growth.

$$\frac{dN_k}{dt} = \left(\frac{dN_k}{dt} \right)_{nucl} + \left(\frac{dN_k}{dt} \right)_{coag} + \left(\frac{dN_k}{dt} \right)_{gr}, \quad k = 1, \dots, N_{bins} \quad (3.28)$$

where, N_{sp} and N_{bins} are total number of gas species and sectional volume bins respectively. The subscripts *nucl*, *coag* and *gr* stand for nucleation, coagulation and growth respectively.

The rate of change of mass fraction of gas phase species is contributed by gas phase chemistry and particle nucleation and growth model.

$$\frac{dY_i}{dt} = \left(\frac{dY_i}{dt}\right)_{gas} + \left(\frac{dY_i}{dt}\right)_{soot}, \quad i = 1, \dots, N_{sp} \quad (3.29)$$

In the model, rates of the gas-phase species and rates of the particle concentration for each bin are calculated at each time-step using the concentrations from the previous time-step. These rate equations are then sent to a stiff ODE solver (CVODE solver by Sundials). The methods used in CVODE are variable-order, variable-step multistep methods. For stiff problems, CVODE includes the Backward Differentiation Formulas (BDFs) in fixed-leading coefficient form, with order varying between 1 and 5 [78, 79].

3.4 Summary

Computational model helps in better understanding of the soot formation process which involves numerous reactions, simultaneous depletion and production of new species and evolution of gas phase species into nano-sized particles. The gas phase reaction mechanism used in this model is given by Slavinskaya et al. [77] which uses 102 species and 807 reactions. The particle model is a discrete sectional model where each section is represented by a representative constant particle size. The change in number concentration of particles due to particle-particle coagulation and pyrene condensation can result in particle sizes which do not match any of the representative sizes of the sections defined. These new particle were assigned to the adjacent sections while conserving the total mass and the number of the new particles. In the model only pyrene was used as the nucleating species contributing to the formation of new particles.

Chapter 4

Results

The soot particle size distribution functions (PSDF) were obtained for oxidation of ethylene in a burner stabilized flat flame (BSFF). In earlier studies [59, 60], measurement of soot PSDFs in BSFF were made by probe sampling followed by particle sizing using a SMPS. A characteristic bimodal distribution was reported with one peak at smaller sizes (3 - 4 *nm*) and another peak at larger sizes.

The objective in this work was to reproduce similar results using the same experimental configuration of soot generation in BSFF and measurement through probe sampling and SMPS. The detailed experimental set-up was described in Chapter 2. The results presented in this chapter agree well with the published work.

The similar probe sampling technique was then used to collect soot particles from atmospheric pressure MFTR and measure PSDF in SMPS. In earlier studies [7, 83], the total soot mass concentrations were reported for ethylene and acetylene pyrolysis at different temperatures and higher residence times (> 1.2 s). In the current work, total soot mass, number concentrations and the soot PSDF are presented for range of temperatures from 1150 to 1200 *K* and smaller residence times from 200 to 600 *ms*. The soot PSDFs are also presented for ethylene oxidation at $\phi = 4.5$ and $\phi = 5.0$. The measured data for both oxidation and pyrolysis cases are then compared to the results obtained from the zero-D sectional aerosol model.

4.1 PSDF from a flat flame burner

4.1.1 Dilution ratio and its effect on measured PSDF

Based on the calibration of orifice flow rate described in Section 2.3, the dilution ratio (f_D) is calculated for the probe with $130\mu m$ orifice using Eq. 4.1 [60] as,

$$f_D = T_r \frac{Q_c}{Q_0} \quad (4.1)$$

where, $T_r = 3.34$ is the ratio of inlet gas temperature ($\sim 1000K$) and the carrier gas (N_2) temperature ($298 K$), Q_c is the flow rate of cold nitrogen ($44 lpm$) at STP and Q_0 is the calculated flow rate of flame gases at inlet temperature ($\sim 1000 K$).

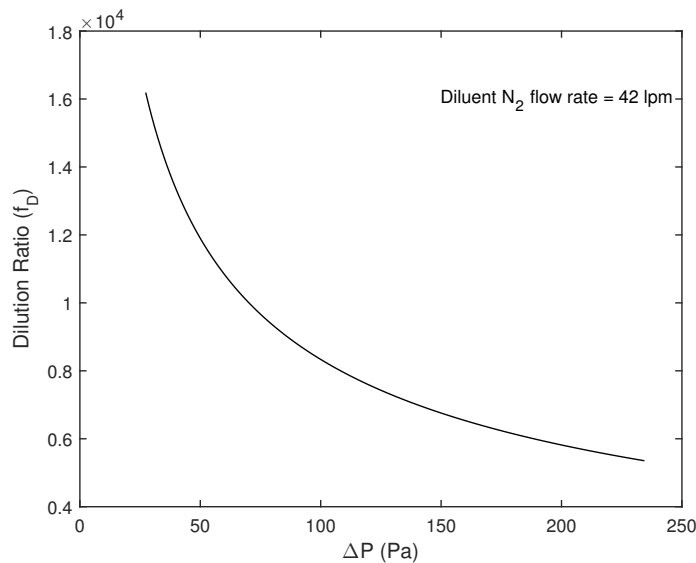


FIGURE 4.1: Variation of dilution ratio (f_D) with the variation in differential pressure across $130\mu m$ orifice for a carrier gas N_2 flow rate of $42 lpm$

As discussed earlier, during online sampling by the SMPS, sampling issues range from particle coagulation and agglomeration to diffusive wall losses in the probe orifice and the sampling line. To minimize these losses, the soot-laden combustion gases must be diluted by a cold non-reacting gas (N_2 in this case). The use of cold N_2 gas helps in immediate quenching of particle growth chemistry and in minimizing the thermophoretic deposition of soot in the sampling line that occurs when high temperature soot-laden gases come in contact with a cold surface [59, 60, 62].

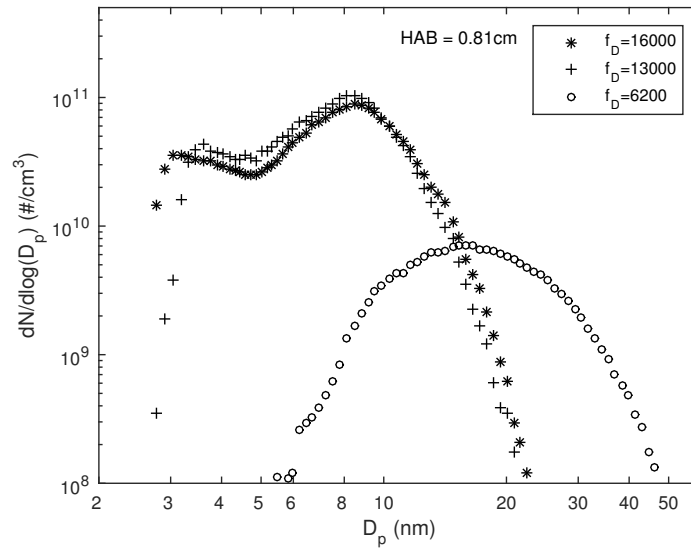


FIGURE 4.2: Absolute PSDF at $HAB = 0.81\text{cm}$ for three dilution ratios at a fixed equivalence ratio, $\phi = 2.1$

In the earlier works by Zhao et al. [59, 60], it was shown that the particle diffusive losses and the particle-particle coagulation can be minimized by systematically increasing the dilution ratio to a critical value where the particles size distribution function becomes independent of the dilution ratio. Experimentally, this critical dilution ratio was of order 1×10^4 . However, other studies have shown that this value can range from 10^3 to 10^4 depending on equivalence ratio and the combustion system [62]. It was also shown [59, 60] that the passage time through orifice of 7ms or less is sufficient to prevent particle losses in the sampling probe.

As demonstrated in Fig. 4.2, the soot size distributions were not affected by increase in dilution ratios above the critical dilution ratio of 1×10^4 . At lower dilution ratios the coagulation is still taking place in the sampling line and, therefore, the peak (mode) at smaller particle sizes disappears due to coagulation of small particles to form larger particles causing the mean diameter to shift to larger particle sizes.

4.1.2 Absolute PSDF

The absolute number density of particles in the flame is related to the SMPS measured number density by,

$$N_a = \frac{f_D}{f_w} N \quad (4.2)$$

where, N_a is the absolute number density of the particles in the flame, f_w is the factor to account for diffusive wall losses and is taken as 1 in this work, N is the soot particle number density measured by SMPS

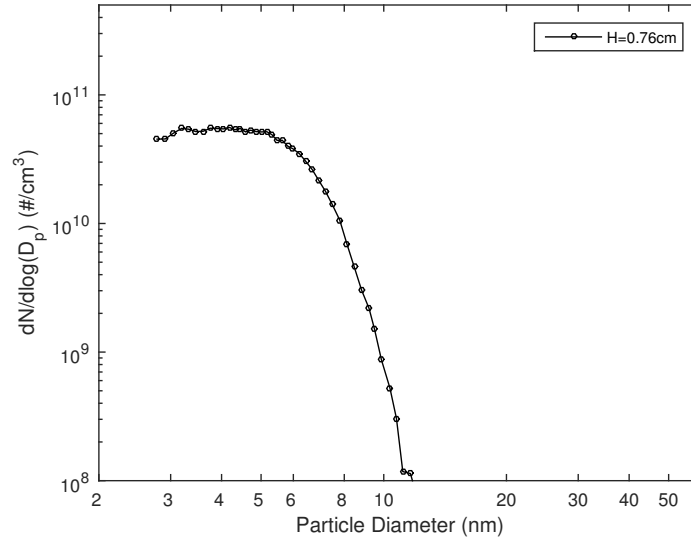


FIGURE 4.3: Absolute PSDF at $HAB = 0.76 \text{ cm}$ at a fixed $\phi = 2.1$

Figure 4.3 presents the soot particle size distribution function at HAB (height above the burner surface) = 0.76 cm where only the particle inception dominates. The mean particle diameter is 4.61 nm . As the height above the burner surface is increased, the mean particle diameter increases and the simultaneous occurrence of soot nucleation and soot particle-particle coagulation are visible as shown in Fig. 4.4.

Figure 4.4 presents the soot PSDF at a relatively larger distance from the burner surface, $HAB = 0.91 \text{ cm}$. As can be seen, the incipient particles are still nucleating (evident from a mode at smaller sizes) while the particles formed earlier have coagulated to form larger size particles, evidenced by a mode at larger diameter. The mean diameter of the distribution is 13.77 nm .

The soot particles size distribution at increasing height above the burner surface, from $HAB = 0.76 \text{ cm}$ to 1.0 cm , are plotted in Fig. 4.5. The mean diameters as a function of HAB are plotted in Fig. 4.6. It is seen that the evolution of PSDFs, from particle inception to growth, is captured in a highly spatially resolved manner.

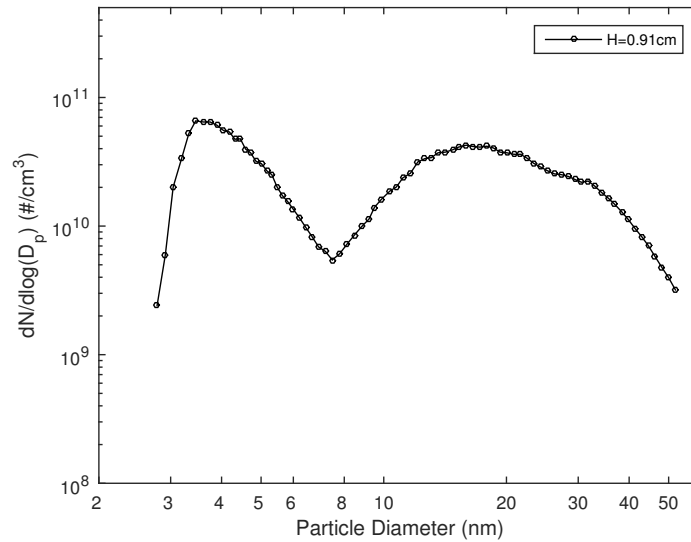


FIGURE 4.4: Absolute PSDF at increasing heights above the burner surface at a fixed $\phi = 2.1$

The soot particles concentration, at height less than 0.75 cm above the burner surface, was either too low or non-existent to be detected by SMPS. At $HAB = 0.76\text{ cm}$, the first PSDF was obtained with a single mode at smaller particle diameter. The mean diameter is 4.61 nm as the soot nucleation is dominant. The nucleation of new particles continues as the height is increased to $HAB = 0.81\text{ cm}$, however, the smaller particles which were formed earlier at lower heights grow into larger sizes due to coagulation and surface growth causing the mean diameter to increase from 4.61 to 7.58 nm . This leads to the formation of second peak in PSDF curve. The second peak becomes more visible at $HAB \geq 0.87\text{ cm}$. This is the characteristic bimodal distribution reported by other studies including Zhao et al. [59–61] in a flat flame at $\phi = 2.1$. At $HAB = 0.87\text{ cm}$, the mode at smaller sizes is still retained, indicative of sustained nucleation, while the coagulation and growth processes continue to increase the mean diameter (13.4 nm) of the soot particles size distribution curve.

The bimodal behavior is present even at larger HAB , however, the particle concentration decreases as the height is increased above 0.91 cm . The mean diameter still keeps increasing to 20.6 nm , due to sustained particle growth through out the flame.

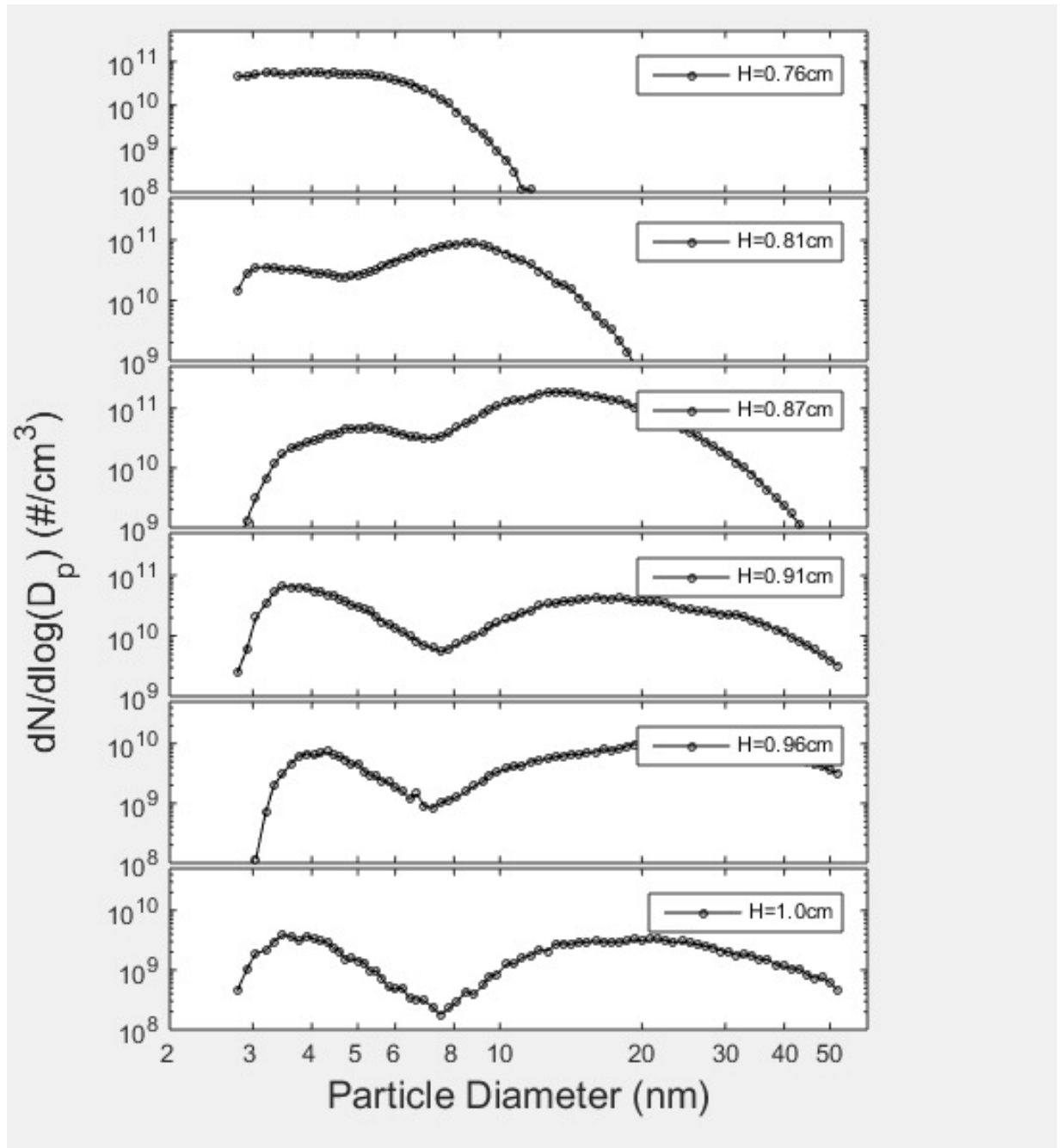


FIGURE 4.5: Absolute PSDF at $HAB = 0.91cm$ at a fixed $\phi = 2.1$

4.2 PSDF from Fuel Pyrolysis in Atmospheric MFTR

4.2.1 Dilution ratio

Based on the calibration of orifice flow rate in Section 2.3, the dilution ratio (f_D) is calculated for the probe with $250\ \mu m$ orifice using Eq. 4.1 [60]. The temperature of the soot-laden hot gases coming out of the tube reactor was measured to be $886K$ when

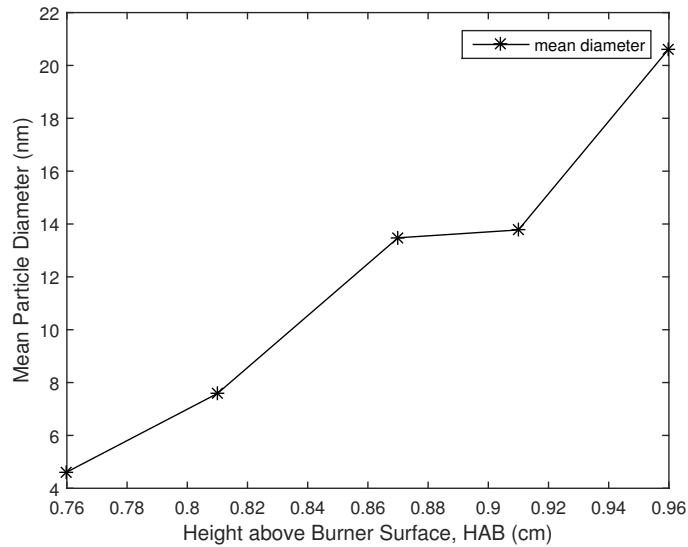


FIGURE 4.6: Mean diameter of soot particles as a function of HAB at a fixed $\phi = 2.1$

the temperature inside the tube reactor was kept constant at $1200K$. Based on this temperature, the temperature ratio, T_r , in Eq. 4.1 was calculated to be 2.97.

As discussed earlier, the dilution is necessary to mitigate particle growth chemistry inside the sampling line and to minimize diffusive wall losses and particle-particle coagulation. The concentration of soot particles at the exit of the reactor depended on the residence time and temperature in MFTR.

Residence time is defined as the time taken by the fuel between the entry of the fuel from the side tubes to the reactor exit. In this work, the residence time is calculated based on the average velocity of the parabolic flow profile in the reactor.

To get the optimum resolution of soot PSDF in SMPS, the flow rate of carrier gas, N_2 , was varied between 10 lpm to 50 lpm . Figure 4.7 presents the dilution ratios obtained for two N_2 flow rates, namely 20 lpm and 40 lpm . The operating differential pressure range in these experiments was varied from 25 to 225 Pa, resulting in the dilution ratio of 500 to 7000, depending on the soot particle concentration obtained at the MFTR exit. The soot particles generated in all the cases of fuel pyrolysis in MFTR were relatively low in concentration due to the presence of 98% N_2 in the MFTR and, therefore, required less probe dilution.

In all the experiments, the dilution ratio was increased till a critical point, after which, further increase in dilution did not affect the soot PSDF and the mean diameter. Figure

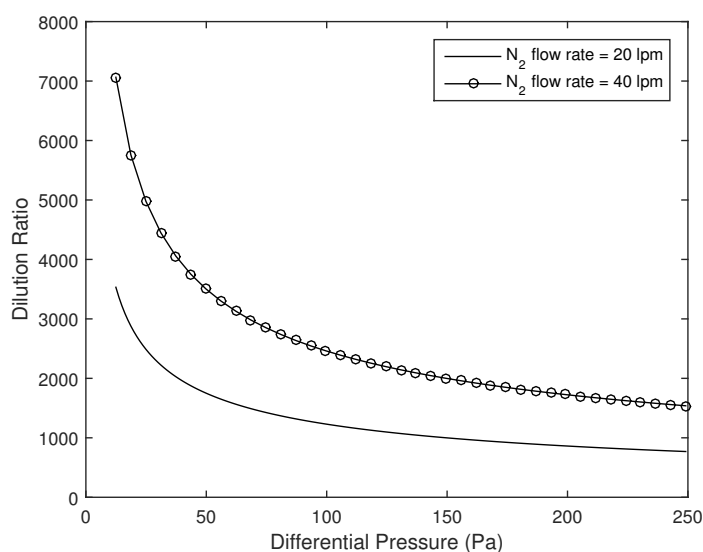


FIGURE 4.7: Variation of dilution ratio with the variation in differential pressure through $250 \mu\text{m}$ orifice for a carrier gas N_2 flow rate of 20 lpm and 40 lpm

4.8 presents the soot PSDF, at MFTR operating conditions of 1200 K and residence time 600 ms , for three dilution ratios. The increase in dilution ratio, above a critical value, did not change the soot PSDF and the mean diameter which was found to be 8.22 nm and 8.34 nm at dilution ratios of 7×10^3 and 5×10^3 respectively.

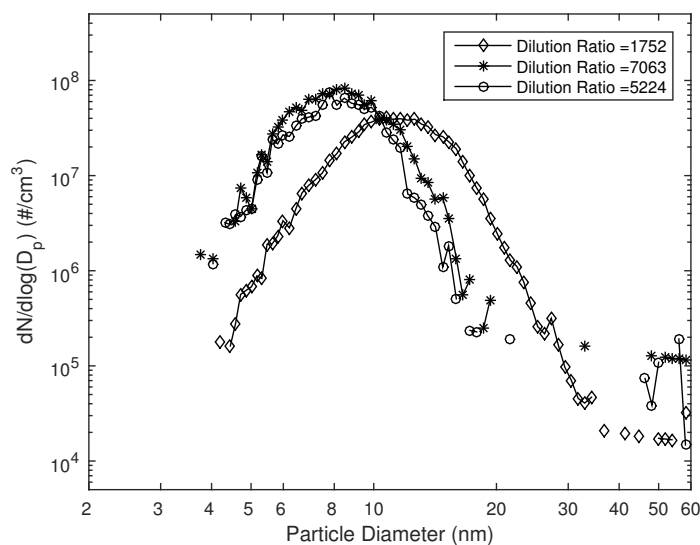


FIGURE 4.8: Soot PSDF obtained from 2% ethylene pyrolysis at 1200 K with residence time of 600 ms inside the MFTR

4.2.2 Absolute PSDFs

The absolute number density of particles obtained from MFTR is related to the SMPS measured number density by Eq. 4.2. Figure 4.9 presents the absolute soot PSDFs for ethylene pyrolysis at 1200 K for a range of residence times from 200 ms to 600 ms. As evident from the figure, the particle number density increases with the increase in residence time in the reactor. The mean diameter of soot PSDF was calculated for each residence time and is presented in Table 4.1.

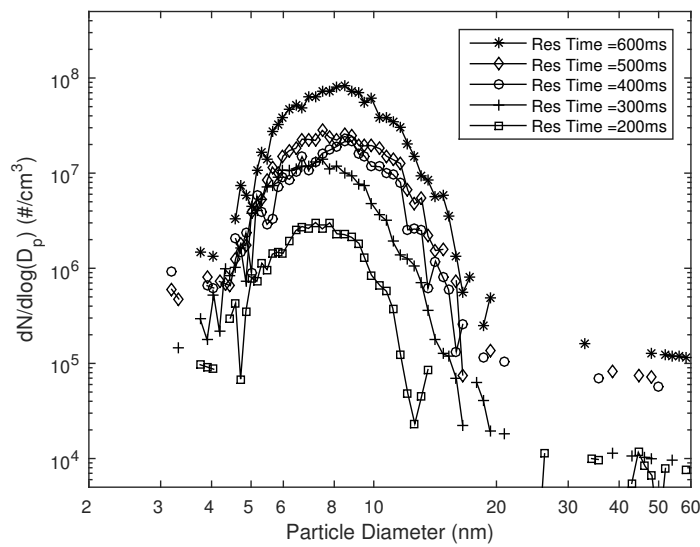


FIGURE 4.9: Soot PSDF for ethylene pyrolysis at 1200 K for a range of residence time

TABLE 4.1: Mean Diameter of the particles at different Residence Times

No	Residence Time (ms)	Mean Diameter (nm)
1	600	8.2471
2	500	8.1902
3	400	8.2525
4	300	7.4496
5	200	7.4178

It is observed that as residence time was increased, the particle concentration also increased but the mean diameter remained almost the same (an increase of ~ 1 nm from

200 to 600ms). The increase in concentration can be attributed to increased nucleation due to longer residence time. The constant mean diameter implies that the soot particle growth processes, including chemical growth and particle-particle coagulation, are not very active at the operating temperature of 1200 K.

Soot PSDFs were also obtained for ethylene pyrolysis at different temperature ranging from 1150 K to 1200 K. The residence time inside the reactor was increased gradually from 160ms to 600ms for each temperature to determine the residence time at which the soot particles concentrations exceeds the threshold of minimum detection limit of SMPS (*i.e.* when the first soot PSDF is obtained in SMPS). Figure 4.10 shows the PSDFs obtained at temperatures ranging from 1150K to 1200 K. The residence times at which the soot PSDFs are detected in SMPS are plotted as a function of temperature in Fig. 4.11, where it is seen that the curve asymptotes at higher temperature. The particle growth is the function of particles number density. As the temperature increases, the number density of incipient particles increases exponentially causing substantial growth and, therefore, explains the asymptotic behavior in Fig. 4.11.

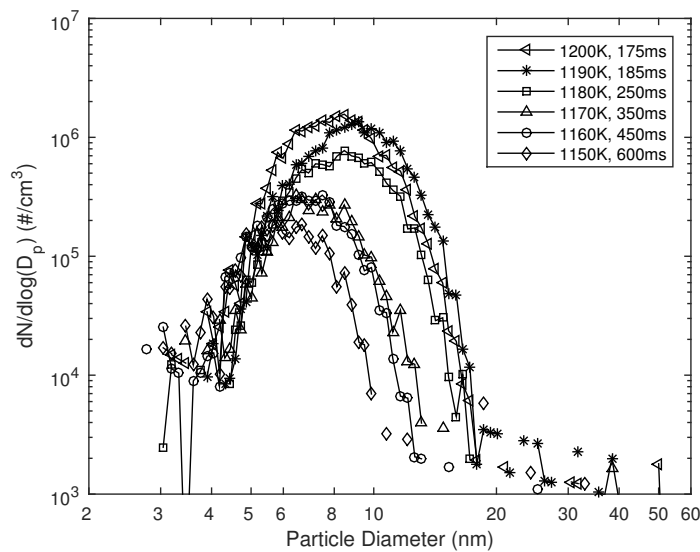


FIGURE 4.10: Soot PSDF obtained at temperatures ranging from 1150 to 1200 K. The residence time is the earliest residence time at which soot PSDF are obtained in SMPS

The soot PSDF at same residence time of 600 ms is compared for 1200 K and 1150 K temperatures in Fig. 4.12. The soot particles concentration is relatively less at lower temperature for same residence time. The increase in the mean diameter at 1200K

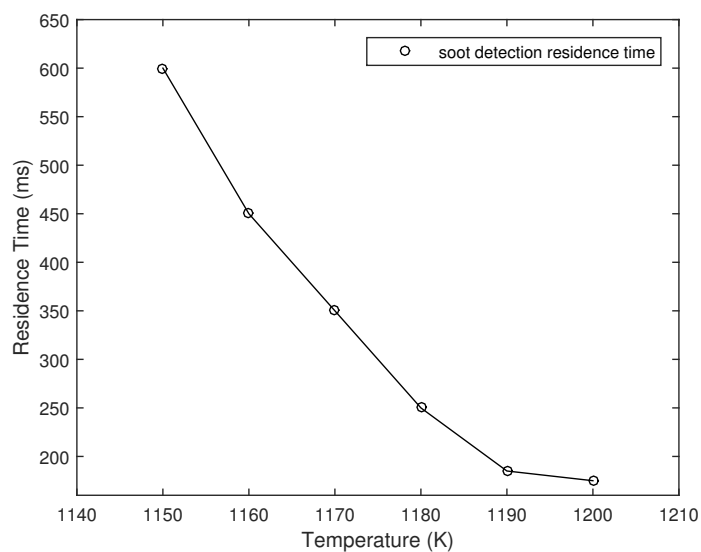


FIGURE 4.11: The earliest residence times at which soot PSDF are obtained in SMPS are plotted as the function of corresponding temperature

temperature can be attributed to higher growth rates due to higher number density of particles at higher temperature.

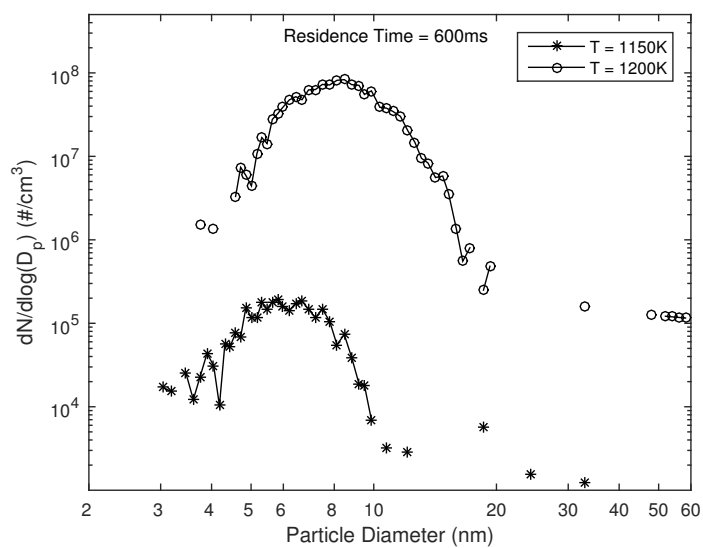


FIGURE 4.12: Soot PSDF obtained from 2% ethylene pyrolysis at 600ms residence time for 1200K and 1150K

4.3 PSDF from Ethylene Oxidation in MFTR

In the same experimental set-up as in Section 4.2, a mixture of air and ethylene in equivalence ratio of 5.0 and 4.5 were mixed with hot nitrogen stream (98%). Figure 4.13 presents the soot PSDF obtained for such partially oxidizing cases under operating condition of 1200 K temperature and 500 ms residence time.

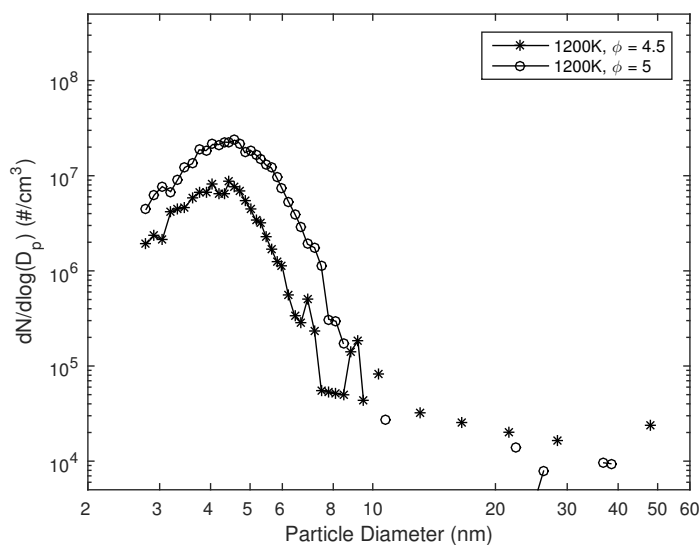


FIGURE 4.13: Soot PSDF obtained for the case of ethylene oxidation at 1200K and 500ms residence time

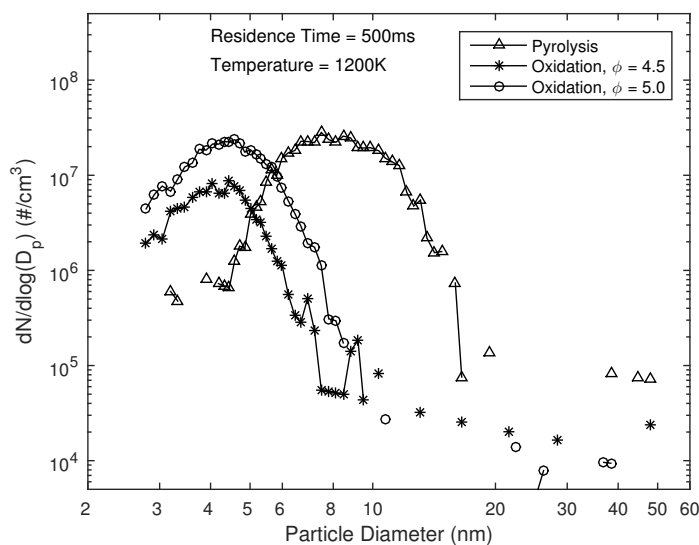


FIGURE 4.14: Comparison of soot PSDF for the cases of ethylene oxidation and pyrolysis

Figure 4.14 presents the comparison of soot PSDF obtained from MFTR under operating condition of 1200K temperature and 500 ms residence time for the cases of pyrolysis as well as oxidation of ethylene in 98% N_2 . The mean diameter for the cases of oxidation with $\phi = 4.5$ and $\phi = 5.0$ are 4.39 nm and 4.64 nm respectively while the mean diameter for the case of fuel pyrolysis is 8.19 nm indicating domination of small particle sizes in the case of oxidation. Earlier studies [24, 44] have proposed the largest effect of oxygen is during the early stages of aromatics growth. This can potentially decrease the soot precursors in the early stages of soot formation resulting in reduction in effective time available for soot growth. Another potential reason is the decrease in soot growth processes (chemical surface growth and particle-particle coagulation) due to low temperature and insufficient H atoms available due to their consumption by O_2 . The behavior captured in soot PSDFs by SMPS is a good indicator of the effect of O_2 on the surface growth of incipient particles.

4.4 Uncertainties in the experiment

The flow profile in the MFTR is laminar, parabolic with radial variation in the flow velocity resulting in radial variation in residence time. However, the residence time is calculated using the average velocity. This radial variation in residence time inside the reactor can result in variable particle growth rates across the cross section of the tube reactor. The diffusion of these particle of different sizes occur throughout through out the length of the reactor and also in the probe orifice. The size of the orifice is relatively very small to the size of the reactor and, therefore, there is an uncertainty as to whether the soot sample entering the probe is a true representation of all the sizes formed in the reactor.

The uncertainty analysis was performed with respect to repeatability, uncertainty of measured data and measurement uncertainties of instruments.

1. The uncertainty in the flow meters is 1%.
2. The uncertainty in thermocouples is 0.75%.
3. The fluctuation in pressure gauge readings is 0.04 in- H_2O .

4. The uncertainty in n-DMA which has been shown to size 60 nm and 100 nm Standard Reference Material (SRM) with an uncertainty of only 1% [84].
5. The uncertainty in n-CPC which varies from 100% to almost 0% as the particle size ($D_p^{mobility}$) is increased from 2 to 3 nm as shown in Fig. 4.15 [5]. In this work, the $D_p^{mobility}$ of particles was always greater than 3 nm .

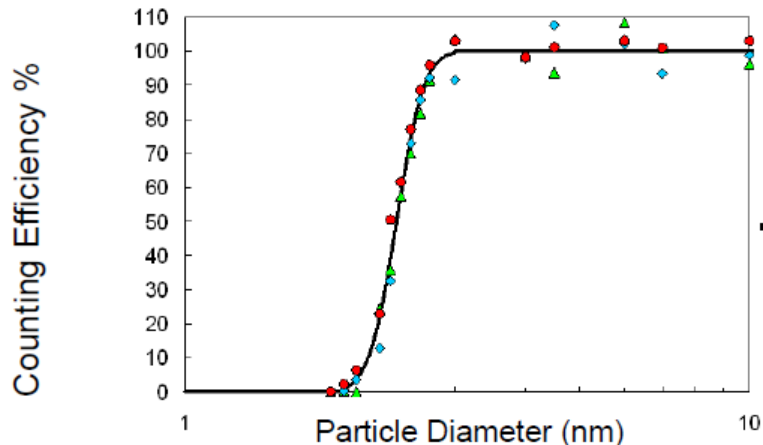


FIGURE 4.15: Counting efficiency curve of CPC [5]

The flow meter uncertainty affects flow rates of N_2 , air, C_2H_4 and orifice flow rate (since the orifice flow rate was calibrated using flow meters). The thermocouple uncertainty affects the temperature inside the tube reactor. The pressure uncertainty affects the orifice flow rate and therefore, the dilution ratios. Three sets of data for both oxidation and pyrolysis were used to calculate the standard deviation from the mean values of number concentration at each particle size to calculate the repeatability uncertainty.

Figure 4.16 and 4.17 presents the PSDF with uncertainties bars for pyrolysis and oxidation of ethylene in MFTR respectively. There is a relatively large uncertainty in PSDFs obtained from ethylene pyrolysis when compared to the oxidation results. The pyrolysis case at 600ms is obtained at a significantly low differential pressure compared to the oxidation case at 500ms resulting in high uncertainty in pressure gauge readings for pyrolysis case.

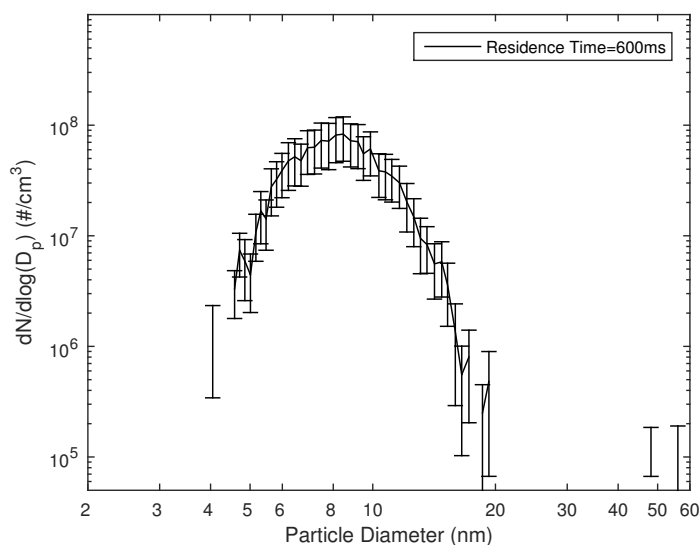


FIGURE 4.16: Soot PSDF and the uncertainty bar at each particle size, obtained from pyrolysis of ethylene at 1200 K and 600 ms residence time

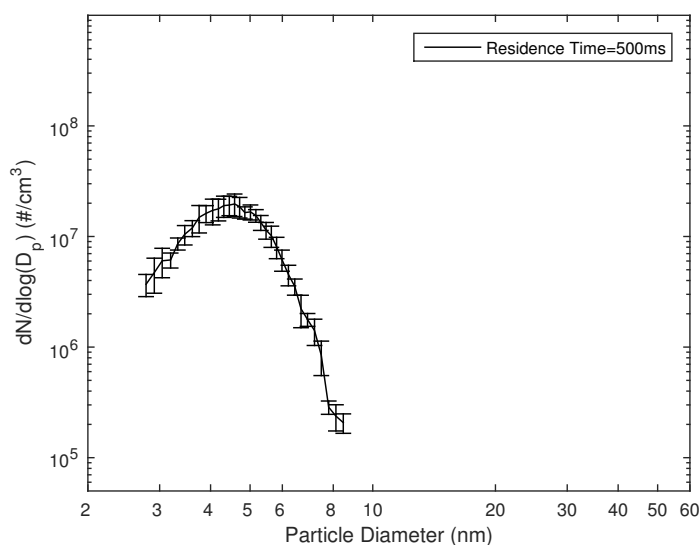


FIGURE 4.17: Soot PSDF and the uncertainty bar at each particle size, obtained from oxidation of ethylene at 1200 K and 500 ms residence time with $\phi = 5.0$

4.5 Results from the Particle Nucleation and Growth Model

The model was run to simulate the conditions in MFTR (Section 4.2 and Section 4.3) for the cases of ethylene pyrolysis and oxidation. The pyrolysis case was run for 98% N_2 and 2% C_2H_4 at 1200 K and the oxidation case was run for 98% N_2 , and 2% of air and C_2H_4 in the equivalence ratio of 4.5 and 5.0 at 1200K. Because the existing SMPS system can

not detect particles having diameter less than $3nm$, the results of the sectional model simulations are presented for particles having diameter greater than $3nm$.

4.5.1 Case1: Pyrolysis

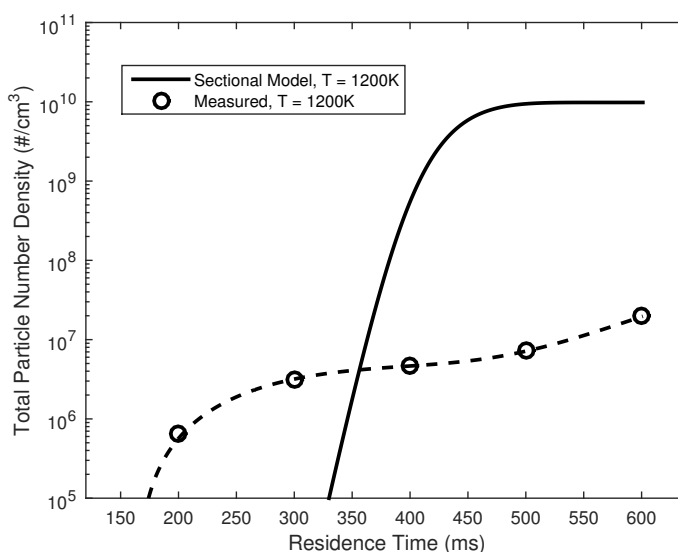


FIGURE 4.18: Total number concentration as a function of residence time for the case of ethylene pyrolysis at 1200K from model simulations and experimental measurements

The total number density of soot particles as a function of residence time is plotted in Fig. 4.18. The results obtained from the model and the experiments show the same trend that the soot particle number concentration increases with the increase in residence time. Both model and experimental results show that the soot formation begins from $200ms$ to $350ms$ in the case of ethylene pyrolysis at $1200K$. The model underpredicts the particles concentration before $350ms$ residence time and overpredicts the particles concentration after $350ms$ residence time. Model prediction of total soot number concentration is 3 order of magnitude higher than the measurements. The similar trend is seen for total soot mass density plotted in Fig. 4.19.

The soot particles size distributions for $600ms$ residence time at $1200K$ are plotted for both the model and the experiments in Fig. 4.20. As seen from the figure, there is no nucleation mode in the experimental results. The potential reason for this can be the flow conditions in the MFTR. The normalized particle size distribution is plotted in Fig. 4.21 which shows similar trends for the model and the measured results. The

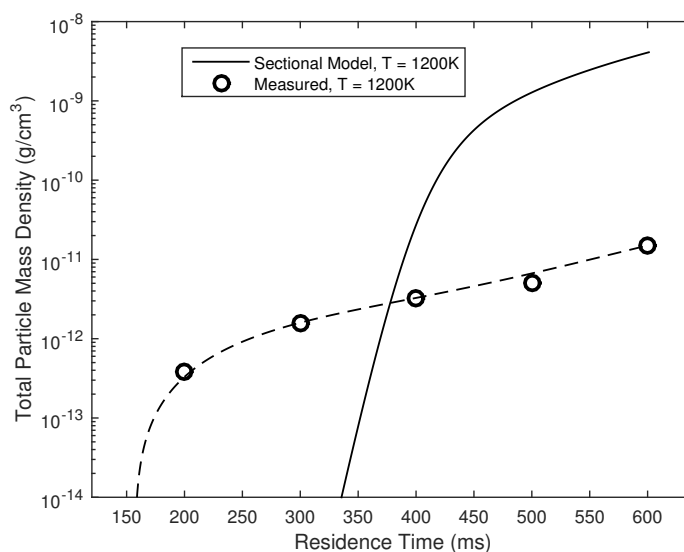


FIGURE 4.19: Total mass concentration as a function of residence time for the case of ethylene pyrolysis at 1200K from model simulations and experimental measurements

mean diameter of soot particles sizes is 6.23 nm and 7.5 nm for the case of model and experimental results respectively.

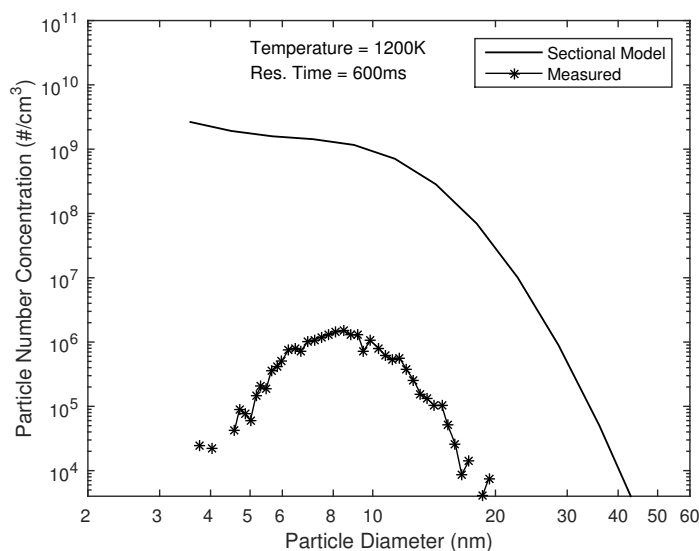


FIGURE 4.20: Soot PSDF obtained for the case of ethylene pyrolysis, at 1200K and 600ms residence time, from model simulations and experimental measurements

4.5.2 Case2: Oxidation

The model results for the two cases of oxidation ($\phi = 4.5$ and $\phi = 5.0$) are presented here. Figure 4.22 compares the particle size distribution, for C_2H_4 oxidation at 1200K and

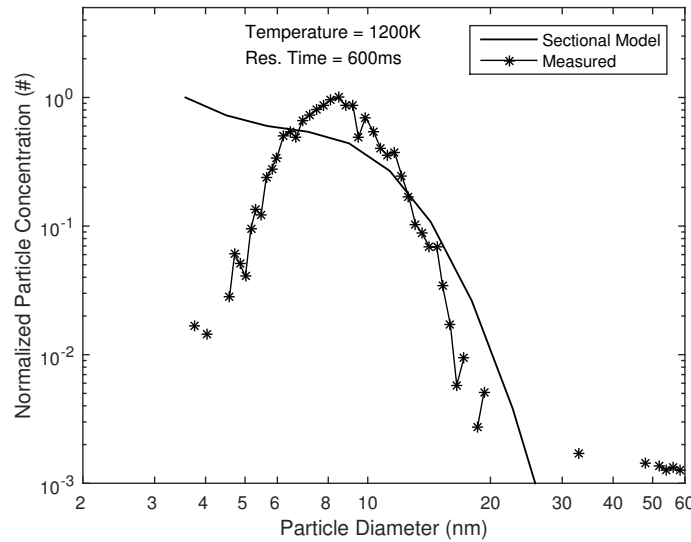


FIGURE 4.21: Normalized soot PSDF obtained for the case of ethylene pyrolysis, at 1200K and 600ms residence time, from model simulations and experimental measurements

500ms residence time, for both the model results and the experimental results. There is a difference of order of $\sim 10^4$ between the modeling and the experimental results.

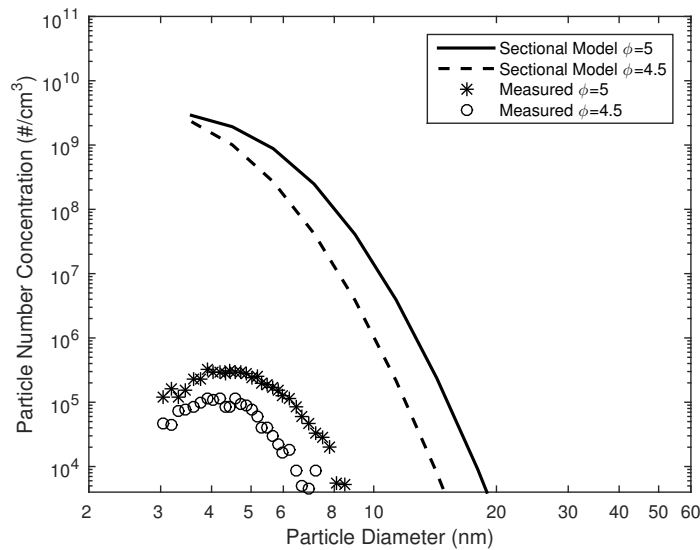


FIGURE 4.22: Soot PSDF at equivalence ratios, 4.5 and 5.0, at 1200K and 500ms residence time, obtained from model simulation and experimental measurements

The normalized particle size distribution for the same operating conditions (1200K, 500ms) are presented in Fig. 4.23. The modeling and the SMPS results have similar trends. The particles concentration decreases as the size increases. The mean diameter in the case of $\phi = 4.5$, is 4.03nm and 4.42nm for the model PSDF and the experiment

PSDF respectively. The mean diameter in the case of $\phi = 5.0$, is $4.36nm$ and $4.65nm$ for the model PSDF and the experiment PSDF respectively. The model results agree well with the experimental results in predicting the size distribution trends.

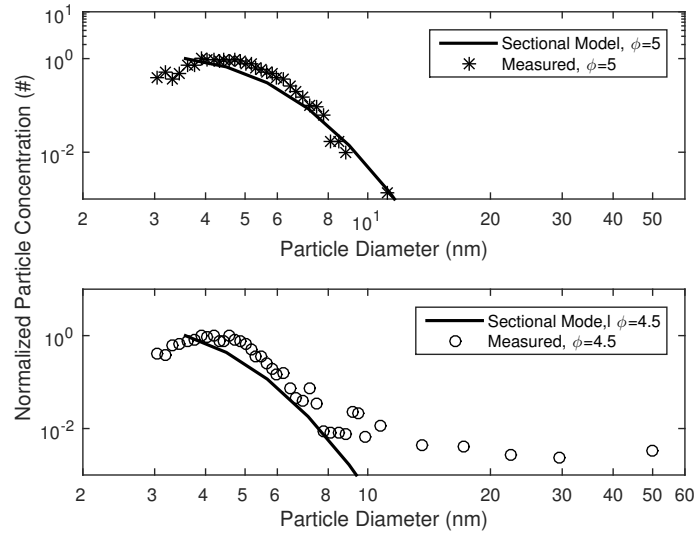


FIGURE 4.23: Normalized soot PSDF at equivalence ratios, 4.5 and 5.0, at 1200K and 500ms residence time, obtained from model simulations and experimental measurements

4.6 Summary

The experimental technique of probe sampling followed by particle sizing using a SMPS was validated by reproducing the literature data on flat flame McKenna burner. At smaller distances from the burner surface ($HAB = 0.76\text{ cm}$), the nucleation of new particles was the only dominant process. As HAB was increased, the single nucleation mode was replaced by a characteristic bimodal distribution in soot PSDFs indicating simultaneous nucleation and coagulation of particles.

Using the similar probe sampling technique, the soot PSDF, total number concentration and total mass of soot particles were measured at different residence times and different temperatures for the cases of pyrolysis and partial oxidation of 2% ethylene in the MFTR.

The residence times were varied from $150ms$ to $600ms$ over a range of temperatures from $1100K$ to $1200K$ to find out the temperatures and the earliest residence times at which the soot particles start forming during pyrolysis of 2% ethylene in the reactor.

The soot particles were first detected at $1150K$ at residence time $600ms$. The earliest residence time of soot particles detection decreased exponentially from $600ms$ to $175ms$ as the temperature increased from $1150K$ to $1200K$ respectively.

The soot PSDFs and particles concentration during pyrolysis of 2% ethylene at $1200K$ at increasing residence times from 200 to 600 ms were measured. It was found that the total soot mass density increased from $3.9 \times 10^{-13} g/cm^3$ at 200 ms residence time to $1.5 \times 10^{-11} g/cm^3$ at 600 ms . For the same case, the total number density increased from $6.45 \times 10^5 \#/cm^3$ to $2.0 \times 10^7 \#/cm^3$ respectively.

The size distribution, total number concentration and total mass of soot particles produced in MFTR were also measured at different equivalence ratios, for the cases of oxidation of ethylene at 500 ms residence time and $1200K$ temperature. The measured results were also compared with the zero-D model for both the cases of pyrolysis and oxidation of ethylene in MFTR.

For the case of pyrolysis, in both the model and the measurements, the mass and the number density of soot particles increased with the increase in residence time at a constant temperature of $1200K$, indicating an increase in nucleation with increase in residence time. The model also agreed with the measured data in predicting the early formation of soot at around 200-350 ms residence time at $1200K$. The measured soot PSDF was a normal distribution with a single mode which was not consistent with the model results that predicted a bimodal distribution at higher residence times (500 ms , 600 ms etc.). The increase in particle mean diameter as a function of residence time was also not significant whereas in the model there was a relatively larger increase in mean diameter with increase in residence times.

The measured data was also compared with the zero-D model for the case of oxidation of ethylene in MFTR. In both the model and the measured results, the modes of size distribution, for the cases of $\phi = 4.5$ and $\phi = 5.0$, were located at smaller sizes indicating low surface growth rates. The normalized size distribution trends obtained from the model and the measured data also agreed well with respect to the mean diameter and the location of the mode of the size distribution.

Chapter 5

Conclusions

SMPS is a high resolution nanoparticle sizer which allows real time online sizing of soot particles obtained from different flow conditions. In the current work, the SMPS system along with probe sampling method was selected to measure soot PSDFs during pyrolysis and oxidation of fuel in atmospheric MFTR. The flow rate through the probe orifice is a function of the thickness of the probe and the orifice diameter and affects the dilution ratio between the incoming hot gases through orifice and the carrier gas nitrogen. The optimum probe thickness and orifice diameter were selected so that the dilution ratio is above the critical value where particle losses due to coagulation are negligible.

The experimental technique of probe sampling followed by particle sizing using a SMPS was validated by reproducing the literature data on flat flame McKenna burner. A characteristic bimodal distribution in soot PSDFs at increasing *HABs* were measured that agreed with the published work.

Using the similar probe sampling technique, the soot PSDF and the total concentration of soot particles were measured at different residence times and different temperatures for the cases of pyrolysis and partial oxidation of 2% ethylene in the MFTR.

The residence times were varied over a range of temperatures to find out the temperature and the earliest residence times at which the soot particles start forming during pyrolysis of 2% ethylene in the reactor. The soot particles were first detected at 1150K at residence time 600ms. The earliest residence time of soot particles detection decreased exponentially from 600ms to 175ms as the temperature increased from 1150K to 1200K

respectively. The soot PSDFs and particles concentration during pyrolysis of 2% ethylene at 1200K at increasing residence times from 200 to 600 *ms* were also measured. It was found that the total soot mass and number density increased with the increase in residence times.

The soot particles formed during partial oxidation of ethylene ($\phi = 4.5$ and $\phi = 5.0$) in 98% nitrogen at 1200 K and 500 *ms* residence time in atmospheric MFTR were also measured to study the effects of oxygen on the particle size distribution and total concentration of soot particles. It was found that the presence of oxygen affects the particle growth rates as the mode of soot PSDF shifted towards the smaller sizes (4 *nm*) when compared with the pyrolysis case (8 *nm*).

The experimental results were also compared with the results from zero-D model for both pyrolysis and oxidation cases. In the pyrolysis case the number density of soot particles increased with increase in residence times in both measured and model results, indicating an increase in nucleation rates with increase in residence times. The model also agreed with the measured data in predicting the early formation of soot at around 200-350 *ms* residence time at 1200K. In the oxidation case, for both the model and the measured results, the modes of size distribution, for the cases of $\phi = 4.5$ and $\phi = 5.0$, were located at smaller sizes indicating low surface growth rates. The normalized size distribution trends obtained from the model and the measured data also agreed well with respect to the mean diameter and the location of the mode of the size distribution.

5.1 Future Work

The measurement of gas phase species produced or consumed during pyrolysis and oxidation of fuel inside MFTR including acetylene, ethylene and larger species like benzene and pyrene will be undertaken in the future work. These measurements will give better understanding of theoretical process of soot formation in various flow conditions and will also help in improving accuracy of sectional aerosol model.

The experimental technique of probe sampling followed by particle sizing using a SMPS, similar to the one used in this work, will also be implemented to measure soot PSDFs during pyrolysis and oxidation of fuels in the high pressure MFTR.

References

- [1] Carlos Andres Echavarria. *Evolution of soot size distribution during soot formation and soot oxidation-fragmentation in premixed flames: experimental and modeling study*. PhD thesis, University of Utah, Department of Chemical Engineering, 2010. Page 3.
- [2] William C Hinds. *Aerosol technology: properties, behavior, and measurement of airborne particles*. New York, Wiley-Interscience, 1982. 442 p., 1, 1982.
- [3] *Operation and service manual for Electrostatic Classifiers, Series 3080*. TSI, March 2009.
- [4] *Operation and service manual for Nano water-based condensation particle counter, Series 3788*. TSI.
- [5] K Erickson, M Singh, and B Osmondson. Measuring nanoparticle size distributions in real-time: Key factors for accuracy.
- [6] Norbert Peters. *Turbulent combustion*. Cambridge university press, 2000.
- [7] MP Ruiz, R Guzman de Villoria, A Millera, MU Alzueta, and R Bilbao. Influence of the temperature on the properties of the soot formed from c 2 h 2 pyrolysis. *Chemical Engineering Journal*, 127(1):1–9, 2007.
- [8] Sverre Vedal. Ambient particles and health: lines that divide. *Journal of the Air & Waste Management Association*, 47(5):551–581, 1997.
- [9] P Minutolo, G Gambi, A D’Alessio, and S Carlucci. Spectroscopic characterisation of carbonaceous nanoparticles in premixed flames. *Atmospheric Environment*, 33(17):2725–2732, 1999.

- [10] Peter R Buseck and MIHAly POsfai. Airborne minerals and related aerosol particles: Effects on climate and the environment. *Proceedings of the National Academy of Sciences*, 96(7):3372–3379, 1999.
- [11] WC Hueper. Environmental carcinogenesis and cancers. *Cancer research*, 21(7):842–857, 1961.
- [12] Edward Goldberg. Black carbon in the environment. 1985.
- [13] Jonathan O Allen, Nameeta M Dookeran, Kenneth A Smith, Adel F Sarofim, Koli Taghizadeh, and Arthur L Lafleur. Measurement of polycyclic aromatic hydrocarbons associated with size-segregated atmospheric aerosols in massachusetts. *Environmental Science & Technology*, 30(3):1023–1031, 1996.
- [14] Debra A Kaden, Ronald A Hites, and William G Thilly. Mutagenicity of soot and associated polycyclic aromatic hydrocarbons to salmonella typhimurium. *Cancer research*, 39(10):4152–4159, 1979.
- [15] Alexander W Wood, Wayne Levin, Richard L Chang, Mou-Tuan Huang, Dene E Ryan, Paul E Thomas, Roland E Lehr, Subodh Kumar, Masato Koreeda, Hirashi Akagi, et al. Mutagenicity and tumor-initiating activity of cyclopenta (c, d) pyrene and structurally related compounds. *Cancer research*, 40(3):642–649, 1980.
- [16] Peter P Fu, Frederick A Beland, and Shen K Yang. Cyclopenta-polycyclic aromatic hydrocarbons: potential carcinogens and mutagens. *Carcinogenesis*, 1(8):725–727, 1980.
- [17] Mikhail F Denissenko, Annie Pao, Moon-shong Tang, and Gerd P Pfeifer. Preferential formation of benzo [a] pyrene adducts at lung cancer mutational hotspots in p53. *Science*, 274(5286):430–432, 1996.
- [18] Eric J Jensen, Owen Toon, et al. The potential impact of soot particles from aircraft exhaust on cirrus clouds. *Geophysical Research Letters*, 24(3):249–252, 1997.
- [19] Veerabhadran Ramanathan and Gregory Carmichael. Global and regional climate changes due to black carbon. *Nature geoscience*, 1(4):221–227, 2008.
- [20] Michael Frenklach and Hai Wang. Detailed modeling of soot particle nucleation and growth. In *Symposium (International) on Combustion*, volume 23, pages 1559–1566. Elsevier, 1991.

-
- [21] Jörg Appel, Henning Bockhorn, and Michael Frenklach. Kinetic modeling of soot formation with detailed chemistry and physics: laminar premixed flames of c 2 hydrocarbons. *Combustion and Flame*, 121(1):122–136, 2000.
- [22] JS Bhatt and RP Lindstedt. Analysis of the impact of agglomeration and surface chemistry models on soot formation and oxidation. *Proceedings of the Combustion Institute*, 32(1):713–720, 2009.
- [23] M Frenklach, WC GARDINER, SE Stein, DW Clary, and T Yuan. Mechanism of soot formation in acetylene-oxygen mixtures. *Combustion science and technology*, 50(1-3):79–115, 1986.
- [24] Michael Frenklach. Reaction mechanism of soot formation in flames. *Physical Chemistry Chemical Physics*, 4(11):2028–2037, 2002.
- [25] Klaus H Homann and H Gg Wagner. Some new aspects of the mechanism of carbon formation in premixed flames. In *Symposium (International) on Combustion*, volume 11, pages 371–379. Elsevier, 1967.
- [26] KH Homann and H Gg Wagner. Chemistry of carbon formation in flames. *Proceedings of the Royal Society of London. Series A, Mathematical and Physical Sciences*, pages 141–152, 1968.
- [27] Hartwell F Calcote. Mechanisms of soot nucleation in flames—a critical review. *Combustion and Flame*, 42:215–242, 1981.
- [28] Michael Frenklach and Hai Wang. Detailed mechanism and modeling of soot particle formation. In *Soot formation in combustion*, pages 165–192. Springer, 1994.
- [29] Kermit C Smyth, J Houston Miller, Robert C Dorfman, W Gary Mallard, and Robert J Santoro. Soot inception in a methane/air diffusion flame as characterized by detailed species profiles. *Combustion and Flame*, 62(2):157–181, 1985.
- [30] Andrea D’Anna, Antonio D’Alessio, and Patrizia Minutolo. Spectroscopic and chemical characterization of soot inception processes in premixed laminar flames at atmospheric pressure. In *Soot formation in combustion*, pages 83–103. Springer, 1994.
- [31] RA Dobbins and H Subramaniasivam. In soot formation in combustion; bockhorn, h., ed, 1994.

- [32] RP Lindstedt and H Bockhorn. Soot formation in combustion: Mechanisms and models. *Springer-Verlag Series in Chemical Physics*, 59:417–441, 1994.
- [33] RD Kern and K Xie. Shock tube studies of gas phase reactions preceding the soot formation process. *Progress in Energy and Combustion Science*, 17(3):191–210, 1991.
- [34] Stephen E Stein, James A Walker, Mahendra M Suryan, and Askar Fahr. A new path to benzene in flames. In *Symposium (International) on Combustion*, volume 23, pages 85–90. Elsevier, 1991.
- [35] Carl F Melius, James A Miller, and Earl M Evleth. Unimolecular reaction mechanisms involving c 3 h 4, c 4 h 4, and c 6 h 6 hydrocarbon species. In *Symposium (International) on Combustion*, volume 24, pages 621–628. Elsevier, 1992.
- [36] Carl F Melius, Michael E Colvin, Nick M Marinov, William J Pit, and Selim M Senkan. Reaction mechanisms in aromatic hydrocarbon formation involving the c 5 h 5 cyclopentadienyl moiety. In *Symposium (International) on Combustion*, volume 26, pages 685–692. Elsevier, 1996.
- [37] Charles S McEnally, Lisa D Pfefferle, Allison G Robinson, and Timothy S Zwier. Aromatic hydrocarbon formation in nonpremixed flames doped with diacetylene, vinylacetylene, and other hydrocarbons: evidence for pathways involving c4 species. *Combustion and flame*, 123(3):344–357, 2000.
- [38] George W Sidebotham and Irvin Glassman. Flame temperature, fuel structure, and fuel concentration effects on soot formation in inverse diffusion flames. *Combustion and flame*, 90(3):269–283, 1992.
- [39] Andrea D’Anna and Angela Violi. A kinetic model for the formation of aromatic hydrocarbons in premixed laminar flames. In *Symposium (International) on Combustion*, volume 27, pages 425–433. Elsevier, 1998.
- [40] A D’Anna, A D’Alessio, and J Kent. A computational study of hydrocarbon growth and the formation of aromatics in coflowing laminar diffusion flames of ethylene. *Combustion and flame*, 125(3):1196–1206, 2001.

- [41] Dorian SN Parker, Ralf I Kaiser, Tyler P Troy, and Musahid Ahmed. Hydrogen abstraction/acetylene addition revealed. *Angewandte Chemie International Edition*, 53(30):7740–7744, 2014.
- [42] Marco J Castaldi, Nick M Marinov, Carl F Melius, Jiamei Huang, Selim M Senkan, William J Pit, and Charles K Westbrook. Experimental and modeling investigation of aromatic and polycyclic aromatic hydrocarbon formation in a premixed ethylene flame. In *Symposium (International) on Combustion*, volume 26, pages 693–702. Elsevier, 1996.
- [43] Christopher J Pope and James A Miller. Exploring old and new benzene formation pathways in low-pressure premixed flames of aliphatic fuels. *Proceedings of the Combustion Institute*, 28(2):1519–1527, 2000.
- [44] Brian S Haynes and H Gg Wagner. Soot formation. *Progress in Energy and Combustion Science*, 7(4):229–273, 1981.
- [45] Marian Von Smoluchowski. Drei vortrage uber diffusion. brownsche bewegung und koagulation von kolloidteilchen. *Z. Phys.*, 17:557–585, 1916.
- [46] Sanjeev Kumar and D Ramkrishna. On the solution of population balance equations by discretization—i. a fixed pivot technique. *Chemical Engineering Science*, 51(8):1311–1332, 1996.
- [47] John H Seinfeld and Spyros N Pandis. *Atmospheric chemistry and physics: from air pollution to climate change*. John Wiley & Sons, 2012.
- [48] NA Fuchs. The mechanics of aerosols 1964. *Pagamon, New York*.
- [49] Sheldon K Friedlander and Dust Smoke. Haze: Fundamentals of aerosol dynamics. *Oxford University Press, New York*, page 308, 2000.
- [50] G Prado, J Jagoda, K Neoh, and J Lahaye. A study of soot formation in premixed propane/oxygen flames by in-situ optical techniques and sampling probes. In *Symposium (International) on Combustion*, volume 18, pages 1127–1136. Elsevier, 1981.
- [51] G. W. Smith. In *Soot in Combustion Systems and Its Toxic Properties*, page 163. Plenum, New York, 1983.

- [52] JA Cole, JD Bittner, JP Longwell, and JB Howard. Formation mechanisms of aromatic compounds in aliphatic flames. *Combustion and Flame*, 56(1):51–70, 1984.
- [53] P Gunter, C Schwarz, G Stiesch, and F Otto. Simulation of combustion and pollutant formation for engine-development. *Editorial Springer, Espana*, 2002.
- [54] T Mendiara, MP Domene, A Millera, R Bilbao, and MU Alzueta. An experimental study of the soot formed in the pyrolysis of acetylene. *Journal of analytical and applied pyrolysis*, 74(1):486–493, 2005.
- [55] Nazly E Sánchez, Alicia Callejas, Angela Millera, Rafael Bilbao, and Maria U Alzueta. Determination of polycyclic aromatic hydrocarbons (pah) adsorbed on soot formed in pyrolysis of acetylene at different temperatures. *Chem Eng Trans*, 22:131–136, 2010.
- [56] Jan P Hessler, Soenke Seifert, Randall E Winans, and Thomas H Fletcher. Small-angle x-ray studies of soot inception and growth. *Faraday discussions*, 119:395–407, 2002.
- [57] JP Hessler, S Seifert, and RE Winans. Spatially resolved small-angle x-ray scattering studies of soot inception and growth. *Proceedings of the Combustion Institute*, 29(2):2743–2748, 2002.
- [58] Hai Wang, Bin Zhao, Barbara Wyslouzil, and Kiril Streletzky. Small-angle neutron scattering of soot formed in laminar premixed ethylene flames. *Proceedings of the Combustion Institute*, 29(2):2749–2757, 2002.
- [59] Bin Zhao, Zhiwei Yang, Murray V Johnston, Hai Wang, Anthony S Wexler, Michael Balthasar, and Markus Kraft. Measurement and numerical simulation of soot particle size distribution functions in a laminar premixed ethylene-oxygen-argon flame. *Combustion and Flame*, 133(1):173–188, 2003.
- [60] Bin Zhao, Zhiwei Yang, Jinjin Wang, Murray V Johnston, and Hai Wang. Analysis of soot nanoparticles in a laminar premixed ethylene flame by scanning mobility particle sizer. *Aerosol Science & Technology*, 37(8):611–620, 2003.
- [61] Bin Zhao, Zhiwei Yang, Zhigang Li, Murray V Johnston, and Hai Wang. Particle size distribution function of incipient soot in laminar premixed ethylene flames:

- effect of flame temperature. *Proceedings of the Combustion Institute*, 30(1):1441–1448, 2005.
- [62] Samuel L Manzello, David B Lenhert, Ahmet Yozgatligil, Michael T Donovan, George W Mulholland, Michael R Zachariah, and Wing Tsang. Soot particle size distributions in a well-stirred reactor/plug flow reactor. *Proceedings of the Combustion Institute*, 31(1):675–683, 2007.
- [63] Stephen William Lasher. *Ultra-fine soot investigation in flames*. PhD thesis, Massachusetts Institute of Technology, 1999.
- [64] Georgios Skillas, Heinz Burtscher, Konstantin Siegmann, and Urs Baltensperger. Density and fractal-like dimension of particles from a laminar diffusion flame. *Journal of colloid and interface science*, 217(2):269–274, 1999.
- [65] M Matti Maricq, Stephen J Harris, and Joseph J Szenté. Soot size distributions in rich premixed ethylene flames. *Combustion and flame*, 132(3):328–342, 2003.
- [66] MA Mueller, TJ Kim, RA Yetter, and FL Dryer. Flow reactor studies and kinetic modeling of the h₂/o₂ reaction. *International Journal of Chemical Kinetics*, 31(2):113–125, 1999.
- [67] U Shrestha, GP Simms, CG Moniruzzaman, and HK Chelliah. High-pressure fuel pyrolysis investigation using a microflow tube reactor. In *53rd AIAA Aerospace Sciences Meeting, Orlando, FL*, 2015.
- [68] Bin Zhao, Kei Uchikawa, and Hai Wang. A comparative study of nanoparticles in premixed flames by scanning mobility particle sizer, small angle neutron scattering, and transmission electron microscopy. *Proceedings of the Combustion Institute*, 31(1):851–860, 2007.
- [69] Michael D Allen and Otto G Raabe. Slip correction measurements of spherical solid aerosol particles in an improved millikan apparatus. *Aerosol Science and Technology*, 4(3):269–286, 1985.
- [70] M Knudsen and S Weber. Resistance to motion of small spheres. *Ann. Phys*, 36(5):981–994, 1911.
- [71] PB Keady, FR Quant, and GJ Sem. A condensation nucleus counter for clean rooms. *Proc. Institute of Environmental Sci., Annual Technical Mtg*, pages 445–451, 1986.

-
- [72] Susanne V Hering, Mark R Stolzenburg, Frederick R Quant, Derek R Oberreit, and Patricia B Keady. A laminar-flow, water-based condensation particle counter (wcpc). *Aerosol Science and Technology*, 39(7):659–672, 2005.
- [73] EO Knutson and KT Whitby. Aerosol classification by electric mobility: apparatus, theory, and applications. *Journal of Aerosol Science*, 6(6):443–451, 1975.
- [74] Zhigang Li and Hai Wang. Drag force, diffusion coefficient, and electric mobility of small particles. i. theory applicable to the free-molecule regime. *Physical Review E*, 68(6):061206, 2003.
- [75] Zhigang Li and Hai Wang. Drag force, diffusion coefficient, and electric mobility of small particles. ii. application. *Physical Review E*, 68(6):061207, 2003.
- [76] Gaetano Esposito. private communication, 2014.
- [77] Nadezhda A Slavinskaya, Uwe Riedel, Seth B Dworkin, and Murray J Thomson. Detailed numerical modeling of pah formation and growth in non-premixed ethylene and ethane flames. *Combustion and Flame*, 159(3):979–995, 2012.
- [78] Alan C Hindmarsh and Radu Serban. User documentation for cvodes, an ode solver with sensitivity analysis capabilities. *Livermore (California): Lawrence Livermore National Laboratory*, 189, 2002.
- [79] Alan C Hindmarsh, Peter N Brown, Keith E Grant, Steven L Lee, Radu Serban, Dan E Shumaker, and Carol S Woodward. Sundials: Suite of nonlinear and differential/algebraic equation solvers. *ACM Transactions on Mathematical Software (TOMS)*, 31(3):363–396, 2005.
- [80] Hai Wang and Michael Frenklach. A detailed kinetic modeling study of aromatics formation in laminar premixed acetylene and ethylene flames. *Combustion and flame*, 110(1):173–221, 1997.
- [81] SH Park and SN Rogak. A novel fixed-sectional model for the formation and growth of aerosol agglomerates. *Journal of aerosol science*, 35(11):1385–1404, 2004.
- [82] Stephen J Harris and Anita M Weiner. Surface growth of soot particles in premixed ethylene/air flames. *Combustion Science and Technology*, 31(3-4):155–167, 1983.

-
- [83] NE Sanchez, A Callejas, A Millera, R Bilbao, and MU Alzueta. Formation of pah and soot during acetylene pyrolysis at different gas residence times and reaction temperatures. *Energy*, 43(1):30–36, 2012.
- [84] George W Mulholland, Michelle K Donnelly, Charles R Hagwood, Scott R Kukuck, Vincent A Hackley, and David YH Pui. Measurement of 100 nm and 60 nm particle standards by differential mobility analysis. *JOURNAL OF RESEARCH-NATIONAL INSTITUTE OF STANDARDS AND TECHNOLOGY*, 111(4):257, 2006.